LA-UR-17-30152 (Accepted Manuscript)

Coupled elasticity, plastic slip, and twinning in single crystal titanium loaded by split-Hopkinson pressure bar

Feng, Biao
Bronkhorst, Curt Allan
Addessio, Francis L.
Morrow, Benjamin Mark
Cerreta, Ellen Kathleen
Lookman, Turab
Lebensohn, Ricardo A.
Low, T.

To be published in: Journal of the Mechanics and Physics of Solids

DOI to publisher's version: 10.1016/j.jmps.2018.06.018

Permalink to record: http://permalink.lanl.gov/object/view?what=info:lanl-repo/lareport/LA-UR-17-30152

Coupled elasticity, plastic slip, and twinning in single crystal titanium loaded by split-Hopkinson pressure bar

B. Feng , C.A. Bronkhorst , F.L. Addessio , B.M. Morrow , E.K. Cerreta , T. Lookman , R.A. Lebensohn , T. Low

PII: S0022-5096(17)31030-X
DOI: 10.1016/j.jmps.2018.06.018
Reference: MPS 3375

To appear in: *Journal of the Mechanics and Physics of Solids*

Received date: 13 November 2017
Revised date: 17 June 2018
Accepted date: 22 June 2018

Please cite this article as: B. Feng , C.A. Bronkhorst , F.L. Addessio , B.M. Morrow , E.K. Cerreta , T. Lookman , R.A. Lebensohn , T. Low , Coupled elasticity, plastic slip, and twinning in single crystal titanium loaded by split-Hopkinson pressure bar, *Journal of the Mechanics and Physics of Solids* (2018), doi: 10.1016/j.jmps.2018.06.018

Coupled elasticity, plastic slip, and twinning in single crystal titanium loaded by split-Hopkinson pressure bar

B. Feng[1], C. A. Bronkhorst[*1], F. L. Addessio[1], B. M. Morrow[1], E. K. Cerreta[1], T. Lookman[1], R. A. Lebensohn[1], T. Low[2]

[1]*Los Alamos National Laboratory, Los Alamos, NM 87545, United States*
[2]*The Ohio State University, Columbus, OH 43218, United States*

Abstract Coupled elasticity, plastic slip, and twinning in high-purity single crystal titanium loaded by split-Hopkinson pressure bar (SHPB) are investigated, in the framework of large deformation and by utilizing the finite element method (FEM). A thermodynamically consistent system of equations for combined plastic slip and twinning is formulated. Novel kinematics is proposed to develop the driving forces for slip and twinning processes and to consider plastic slip in twins. Dislocation based crystal plasticity is proposed, with an emphasis on the interactions among all slip modes in multi-variant/multiphase heterogeneous materials. A mechanism for dislocation density evolution during twinning is proposed. The impact loading along the [0001] and $\left[10\bar{1}1\right]$ directions of single crystal high purity titanium is investigated. The evolution of stress-strain field, dislocation density, and volume fraction for each variant in the sample during the entire loading process are obtained and discussed in detail. Results in simulations show that for the [0001] specimen due to the existence of six symmetry primary twin variants with respect to the loading direction and fifteen different slip systems in each variant, the fields of stress and dislocation density are very homogenous in the sample. The simulation results are compared with experimental data for the [0001] and $\left[10\bar{1}1\right]$ specimens. The experimental results are explained and interpreted for both specimens, which include the pole figures, the stress-strain curves, and volume fraction of variants. The simulation results provide an important insight into mechanical responses of high-purity single crystal titanium under high rate loading, and this paper advances the mesoscale modeling and simulations in coupled plastic slip and twinning.

Keywords: dislocation based crystal plasticity, deformation twinning, large deformation, high strain rate loading

[*] Corresponding author.
Emails: cabronk@lanl.gov (C. A. Bronkhorst); fengbiao11@gmail.com (B. Feng).

1. Introduction

Understanding of material behaviors under the extreme environments of high stress and high strain rate loading is of great interest and critical to material applications in automotive, space and aeronautic, nuclear, and defense industries. Hexagonal close-packed (HCP) metals such as titanium, zirconium, magnesium, and their alloys have widespread applications (Feng and Levitas, 2017c). In the case of HCP titanium, it has highly attractive properties such as low density, high strength-to-weight ratio, relatively high melting point, high biocompatibility, good deformability at high temperature, and excellent corrosion resistance (Hama et al., 2017; Wang, 1996; Zeng et al., 2009). Split-Hopkinson pressure bar (SHPB) has been widely used to investigate dynamic compression properties of solid materials at the strain rates between 10^2 and 10^4 s^{-1} (for a brief review, see (Gray, 2000; Frew et al., 2005; Gama et al., 2004)). In addition, the plate impact experiment is also commonly used to study material behaviors under shock loading, in which the peak strain rate is typically between 10^5 and 10^7 s^{-1} and velocimetry is frequently employed to measure sample responses. Recently, polycrystal zirconium (Cerreta et al., 2013; Escobedo et al., 2012; Morrow et al., 2017a; Rigg et al., 2009; Song and Gray, 1995) and titanium (Bezruchko et al., 2006; Morrow et al., 2017a), and single crystal titanium (Morrow et al., 2017b) under shock loading in plate impact experiments have been attracting researchers' interests. The responses of materials to such loading conditions involve very complex physical processes at multi-scales of both length and time such as the nucleation of voids and their subsequent growth, plastic slip in different slip modes and their interactions, the nucleation and growth of twins and martensitic phases, the formation of shear bands, etc. Mesoscale modeling can be used to model the deformation and texture evolution of polycrystals, taking into account the characteristics of the single crystal and polycrystal, serving as a bridge between evolutions of microscale structures (e.g. dislocation propagations and movements) and macroscale deformation, damage and failure.

The sophistication of mesoscale modeling for representation of the deformation and microstructure evolution in HCP materials originates from the coupled multiple physical responses (elasticity, plastic slip, twinning, and phase transformations) and the anisotropy during these responses. Specifically, for elasticity, there are more elastic constants than for cubic symmetry materials. For plastic slip and twinning, anisotropy exists due to slip/twinning modes on different planes and along different directions. For stress-induced phase transformation, the

transformational strain is not purely volumetric but tensorial, and the pathway from HCP to hexagonal crystal structure in titanium is still an ongoing research topic (Trinkle, et al., 2003; Zong, et al., 2014). For HCP metals, plastic slip and twinning can easily occur under dynamic loading conditions, while phase transformation $(\alpha \to \omega)$ does not take place until the stress conditions are high enough. Morrow et al. (2016) experimentally found that plastic slip and twinning in the absence of $\alpha \to \omega$ phase transformation are dominant in high-purity single crystal titanium deformed by SHPB; while phase transformation occurs under shockwave loading with a much higher strain rate and stress than under SHPB (Jones et al., 2017; Mescheryakov et al., 2000). Similar responses are also observed in zirconium under dynamic loading (Cerreta et al., 2013) and demonstrates retained high pressure phase upon unloading. Coupled plastic slip and twinning without phase transformation under SHPB are the focus of this paper and the phase transformation in titanium in plate impact experiment will be investigated in the future.

Mesoscale modeling of the coupled plastic slip and twinning in HCP metals has been an active research area for some time, where a critical resolved shear stress is commonly assumed for each slip and twin mode. Kalidindi (1998) was one of the first to formulate a model to incorporate deformation twinning into a crystal plasticity theory and applied to the polycrystal via a Taylor model, which is widely used and cited in the literature. Salem et al. (2003, 2005) studied the role of deformation twinning in HCP titanium and formulated a model for coupled twinning and dislocation slip based processes. Tomé et al. (2001) developed a polycrystal constitutive description for pure zirconium deforming under quasi-static conditions, where plastic slip and twinning at room and liquid nitrogen temperatures are investigated. Beyerlein and Tomé (2008) developed a single crystal constitutive law accounting for both twinning and dislocation-based slip for zirconium including temperature effects. Abdolvand et al. (2011) incorporated twinning into a crystal plasticity finite element model and investigated the evolution of lattice strains and texture in the HCP Zircaloy-2 under uniaxial tension/compression loading. Wang et al. (2013) proposed a physics-based twinning and de-twinning model for HCP crystals that has the capability of dealing with both mechanisms during plastic deformation. Kumar et al. (2015) modified a full-field elasto-viscoplastic formulation based on fast Fourier transformation and presented a numerical study of the distribution of the local stress state associated with deformation twinning in magnesium. Further, they employed this model to study the effect of

alloying addition on twin thickening and twin transmission in HCP magnesium (Kumar et al., 2017). Zecevic et al. (2015) studied the strain rate and temperature effects on the selection of primary and secondary slip and twinning systems in HCP zirconium. Morrow et al. (2016) modeled plastic slip and twinning in high purity titanium under SHPB loading using a self-consistent homogenization model. Hama et al. (2017) investigated the anisotropic deformation behavior in a commercially pure titanium Grade 1 sheet by coupling crystal plasticity with twinning. Cheng and Ghosh (Cheng et al., 2018; Cheng and Ghosh, 2015, 2017; Ghosh and Cheng, 2018) developed an advanced, image-based crystal plasticity FEM model, for predicting twin formation and associated heterogeneous deformation in magnesium. In addition to HCP materials, the coupled twinning and slip in TWIP steel were studied by Sun et al. (2016, 2017) and in FCC materials in the work of Kalidindi (2001), Staroselsky and Anand (1998) and Wong et al. (2016).

In addition to pseudo-slip modeling for twinning where the twin evolution is driven by a shear stress along the twinning direction as mentioned above, recent polycrystal plasticity work has treated twinning as a statistical process. This process is represented as one where twin nucleation, propagation, and expansion characterize the elements of deformation twinning. Indeed, these three elements of twinning in polycrystal HCP materials are strongly influenced by the statistical distributions of grain size, grain orientation, grain boundary length, grain boundary disorientation angle, twin thickness, twin variant, and loading conditions. An in-depth statistical analysis of these effects using EBSD data can be found in Capolungo et al. (2009). Beyerlein and Tomé (2010) and Beyerlein et al. (2010) presented a basic probabilistic theory for the nucleation of deformation twins in HCP polycrystalline metals, where the grain boundary defects under stress is considered as the controlling mechanism. Beyerlein et al. (2010, 2011) and Beyerlein and Tomé (2010) further developed a multiscale constitutive model for polycrystalline zirconium and magnesium that includes this probabilistic model. Niezgoda et al. (2013, 2014) introduced grain boundary influenced stochastic effects into the viscoplastic self-consistent crystal plasticity framework and applied to twin nucleation in HCP metals. It has been known for many years through polycrystal plasticity work, the important role of deformation and stress heterogeneity (e.g. Kalidindi et al., 1992; Bronkhorst et al, 1992, 2007, 2010, ; Hansen et al., 2010; 2013; Mayeur et al, 2013; Lieberman et al, 2016). The interaction between twin and parent pairs have indicated that neighboring grains can play a significant role in stress evolvement inside the twin

and even in thickening of twins (Abdolvand and Daymond, 2013; Abdolvand et al., 2016; Arul et al., 2016; Bieler et al., 2014). Recently, three-dimensional crystal plasticity finite element (CPFE) models (Addolvand et al., 2015a and 2015b) were developed to consider interaction of twin and parent grains in hcp polycrystal, in which the grain morphologies and microstructures are based on the three-dimensional x-ray diffraction microscopy. Ardeljan et al. (2015) presented an approach to modeling the morphological and crystallographic reorientation associated with the formation and thickening of a twin lamella within a CPFE framework, which captures grain-to-grain interactions and their effect on the mechanical fields. The papers discussed above are focused on the polycrystal materials, and not applied directly to single crystals. Yu et al. (2010) experimentally studied the strong crystal size effect on deformation twinning in single-crystal Ti alloy. Zhang et al. (2014) presented an analytical model to investigate the stochastic size effects on the critical stress for slip and twinning in HCP single crystals. The size effects due to twin appearance on the critical stress for twinning is also considered in the constitutive equations while it is not considered in a stochastic way. The statistical representation of other effects such as loading conditions, temperature, etc. and their influence on twinning within single crystal HCP materials, in the context of high deformation rate loading is still an ongoing research area. The continued development of new experimental capabilities in this field is also necessary for the further development of single crystal plasticity theory. Therefore, we used the pseudo-slip model for twinning in this paper.

It is known that both plastic slip and deformation twinning are dissipative processes (i.e., entropy increases during slip and twinning). The definitions of the resolved shear stresses for the slip and twin modes vary in literature but it was not discussed or proven whether or not these resolved shear stresses are thermodynamically consistent and lead to dissipative processes for both twinning and slip. The critical resolved shear stresses are defined as the double contraction between the Schmid tensor associated with slip/twinning systems and different stress tensors. For example, the Cauchy stress (e.g. in Sun et al., (2016)), second Piola-Kirchhoff stress (e.g. in Salem et al., (2005)), and the Kirchhoff stress (e.g. in Abdolvand et al., (2011)) are commonly used in literature. However, the theory should be always thermodynamically consistent. This is especially true for high deformation rate loading conditions considered here. For the large deformation model and dynamic loading, the resolved shear stresses for slip and twinning in a thermodynamically consistent theory in this paper can be different from other definitions in the

literature. Specifically, as shown in Section 3 of this paper the resolved shear stress for twinning $\tau_{tw-i} = \mathbf{F}_{sl}^{-1} \cdot \mathbf{F}_e^{-1} \cdot \boldsymbol{\sigma} \cdot \mathbf{F}_e \cdot \mathbf{F}_{sl} : \mathbf{b}_i \otimes \mathbf{n}_i$ and for slip $\tau_{\beta i} = \mathbf{F}_e^{-1} \cdot \boldsymbol{\sigma} \cdot \mathbf{F}_e : \left(\mathbf{s}_{\beta i} \otimes \mathbf{m}_{\beta i} \right)$ can be affected by the elastic $\mathbf{F}_e$ and plastic slip $\mathbf{F}_{sl}$ deformation significantly, where deformation in elasticity and slip are finite. The coupling between plastic work and thermal energy due to dissipation is also an essential feature of a theory for dynamic loading conditions. The thermodynamics of slip and twinning is still very much a research area. In addition, as discussed in Section 3, by using the definitions of resolved shear stresses in literature to obtain the dissipation rate, one can always apply the load in a way causing a negative dissipation rate for both slip and twinning, which does not obey the second law of thermodynamics. Therefore, it is necessary and important to develop thermodynamically consistent resolved shear stresses for twinning and slip, which strictly obey the second law of thermodynamics for general three-dimensional loading conditions. The first goal of this paper is to formulate a thermodynamically consistent system of equations in the framework of large deformation, in which the novel definitions for resolved shear stresses strictly obey the second law of thermodynamics. To reach this goal, novel kinematics for plastic slip and twinning is proposed and implemented in thermodynamic laws to develop the driving forces for plastic slip and twinning. Specifically, we multiplicatively decompose the plastic deformation gradient $\mathbf{F}_p$ into twinning $\mathbf{F}_{tw}$ and slip $\mathbf{F}_{sl}$ components: $\mathbf{F}_p = \mathbf{F}_{sl} \cdot \mathbf{F}_{tw}$. In literature, the deformation gradient $\mathbf{F}_p$ in the theories of crystal plasticity are generally not decomposed into a multiplication of two separate configurations of $\mathbf{F}_{sl}$ and $\mathbf{F}_{tw}$. Instead, these two plastic mechanisms are considered in a combined way by the plastic velocity gradient $\dot{\mathbf{F}}_p \cdot \mathbf{F}_p^{-1}$ in the unloaded intermediate configuration (e.g. (Kalidindi, 1998)). Without the multiplicative decomposition of $\mathbf{F}_p$, it is difficult to obtain the correct resolved shear stress for either plastic slip or twinning to strictly obey the second law of thermodynamics, especially when more complicated physics is involved such as phase transformation. In this sense, it is more reasonable to separate these two configurations.

The second goal of this paper is to formulate a dislocation based crystal plasticity theory for multi-variant systems, with emphasis on interactions among all slip modes in all twin variants and also with emphasis on the evolution of dislocation density during twinning. Hansen et al. (2013) formulated a continuum theory to consider the interactions of different types of

dislocation populations in all slip systems of the single crystal material, where twinning is not considered. The current work will advance this theory so that it can be applied in multi-variant or multiphase materials. In addition, we will introduce a new mechanism for dislocation density evolution during twinning, over that proposed in the work by Hansen et al. (2013).

The third goal for this paper is to use high-purity single crystal titanium loaded by SHPB as a case study by using both the system of equations formulated in this paper and the finite element method (FEM) to investigate the mechanical responses in the titanium sample under dynamic loading conditions. In addition, the simulation results will be used to compare with experimental data and reproduce the experimental stress response and evolution of structure. The simulation results also help to explain and interpret the physics behind the observed SHPB experimental results.

At the outset, we define the notation used in this paper. Vectors and tensors are designated with boldface symbols. Contractions of the second-order tensors $\mathbf{H} = \{H_{kl}\}$ and $\mathbf{Q} = \{Q_{mn}\}$ over one and two indices are designated as $\mathbf{H} \cdot \mathbf{Q} = \{H_{ij} Q_{jk}\}$ and $\mathbf{H} : \mathbf{Q} = \{H_{ij} Q_{ji}\}$, respectively. Similarly, we define contractions of the forth-order tensor $\mathbf{K}$ and second-order tensor $\mathbf{Q}$, over one and two indices as $\mathbf{K} \cdot \mathbf{Q} = \{K_{klmn} Q_{no}\}$ and $\mathbf{K} : \mathbf{Q} = \{K_{klmn} Q_{nm}\}$.

2. Kinematics

As usual, the motion of a material with large elastoplastic deformation is described by a continuous vector function $\mathbf{r} = \mathbf{r}(\mathbf{r}_0, t)$, where $\mathbf{r}_0$ and $\mathbf{r}$ are the position vectors of material points in the reference (undeformed) configuration Ω_0 at the time instant t_0 and in the actual (deformed) configuration Ω at the time instant t, respectively. The deformation gradient $\mathbf{F} = \dfrac{\partial \mathbf{r}}{\partial \mathbf{r}_0}$ can be multiplicatively decomposed into elastic $\mathbf{F}_e$ and plastic $\mathbf{F}_p$ parts:

$$\mathbf{F} = \mathbf{F}_e \cdot \mathbf{F}_p = \mathbf{R}_e \cdot \mathbf{U}_e \cdot \mathbf{F}_p, \tag{1}$$

where $\mathbf{U}_e$ is the symmetric elastic right stretch tensor, and $\mathbf{R}_e$ is the proper orthogonal elastic rotation tensor. There are two different mechanisms: slip and twinning contributing to the plastic deformation $\mathbf{F}_p$. To the best of our knowledge, the deformation gradient $\mathbf{F}_p$ in the theories of crystal plasticity in literature is not generally decomposed into a multiplication of two separate

configurations: the plastic slip $\mathbf{F}_{sl}$ and plastic twinning $\mathbf{F}_{tw}$. Instead, these two plastic mechanisms are taken into account in a combined way by the velocity gradient $\dot{\mathbf{F}}_p \cdot \mathbf{F}_p^{-1}$ in the unloaded intermediate configuration (e.g. (Kalidindi, 1998)),

$$\dot{\mathbf{F}}_p \cdot \mathbf{F}_p^{-1} = \mathbf{L}_{sl} + \mathbf{L}_{tw} = \mathbf{L}_{sl-0} + \mathbf{L}_{sl-twins} + \mathbf{L}_{tw}, \tag{2}$$

where $\mathbf{L}_{sl}$ and $\mathbf{L}_{tw}$ are the velocity gradients from plastic slip and twinning, respectively. $\mathbf{L}_{sl}$ can be further decomposed into the contributions from the parent untwinned variant $\mathbf{L}_{sl-0}$ and product twinned variants $\mathbf{L}_{sl-twins}$. Plastic slip in twinned variants sometimes are not considered (i.e. $\mathbf{L}_{sl-twins} = 0$) (e.g. Morrow et al., 2016; Salem et al., 2005; Sun et al., 2016). We will however consider slip in the primary twinned regions of material in this work.

Resolved shear stresses for both slip and twinning should lead to a nonnegative dissipation rate (i.e. a nonnegative increase in entropy) during plastic deformation, which were not proven and studied in past pioneering crystal plasticity theories. For the purpose of developing thermodynamically consistent theory in Section 3, we use the decomposition, $\mathbf{F}_p = \mathbf{F}_{sl} \cdot \mathbf{F}_{tw}$ into slip $\mathbf{F}_{sl}$ and twinning $\mathbf{F}_{tw}$ components. Consequently, the total deformation gradient can be multiplicatively decomposed into

$$\mathbf{F} = \mathbf{F}_e \cdot \mathbf{F}_p = \mathbf{F}_e \cdot \mathbf{F}_{sl} \cdot \mathbf{F}_{tw} = \mathbf{R}_e \cdot \mathbf{U}_e \cdot \mathbf{F}_{sl} \cdot \mathbf{F}_{tw}. \tag{3}$$

Without multiplicative decomposition $\mathbf{F}_p = \mathbf{F}_{sl} \cdot \mathbf{F}_{tw}$ or $\mathbf{F}_p = \mathbf{F}_{tw} \cdot \mathbf{F}_{sl}$, it is difficult to obtain the correct resolved shear stress for either plastic slip or twinning to strictly obey the second law of thermodynamics. In addition, twinning can be viewed as a special form of phase transformation, with a lattice rotation but without the associated change in crystal structure. It is very common to see both $\mathbf{F} = \mathbf{F}_e \cdot \mathbf{F}_t \cdot \mathbf{F}_p$ (e.g. Levitas and Javanbakht (2015)) and $\mathbf{F} = \mathbf{F}_e \cdot \mathbf{F}_p \cdot \mathbf{F}_t$ (e.g. Addessio, et al. (2017)) expressions in literature, where $\mathbf{F}_t$ is the transformational deformation gradient.

As long as we have multiplicative decomposition of $\mathbf{F}_p = \mathbf{F}_{sl} \cdot \mathbf{F}_{tw}$ or $\mathbf{F}_p = \mathbf{F}_{tw} \cdot \mathbf{F}_{sl}$, we can achieve the thermodynamically consistent theory by using the derivation process in Section 3. Both sequences are frequently used in literature. The sequence $\mathbf{F}_p = \mathbf{F}_{sl} \cdot \mathbf{F}_{tw}$ is used in this paper because we consider the plastic slip in twins and *the plastic deformation in twins is after twins are formed*. It is noted that $\mathbf{F}_p = \mathbf{F}_{tw} \cdot \mathbf{F}_{sl}$ is also admissible and has its own advantages as well.

The key point here is to use the multiplicative decomposition of $\mathbf{F}_{sl}$ and $\mathbf{F}_{tw}$ to obtain the resolved shear stresses (the driving forces for slip and twinning), while they are calculated from the double contraction of Schmid tensor of slip/twinning and Cauchy stress/second Piola-Kirchhoff stress/transformed Cauchy stress/Kirchhoff stress in literature for the different configurations.

The velocity gradient $\mathbf{L} = \dot{\mathbf{F}} \cdot \mathbf{F}^{-1} = \mathbf{W} + \mathbf{D}$ is decomposed into the skew-symmetric spin tensor $\mathbf{W} = (\mathbf{L})_a$ and the symmetric deformation gradient rate $\mathbf{D} = (\mathbf{L})_s$, where the subscripts *s* and *a* mean symmetrization and skew-symmetrization of a tensor. Combining with Eq. (3), **L** and **D** can be decomposed into elastic, slip and twinning contributions:

$$\dot{\mathbf{F}} = \dot{\mathbf{F}}_e \cdot \mathbf{F}_{sl} \cdot \mathbf{F}_{tw} + \mathbf{F}_e \cdot \dot{\mathbf{F}}_{sl} \cdot \mathbf{F}_{tw} + \mathbf{F}_e \cdot \mathbf{F}_{sl} \cdot \dot{\mathbf{F}}_{tw}; \qquad \mathbf{F}^{-1} = \mathbf{F}_{tw}^{-1} \cdot \mathbf{F}_{sl}^{-1} \cdot \mathbf{F}_e^{-1}; \tag{4}$$

$$\boldsymbol{L} = \dot{\mathbf{F}} \cdot \mathbf{F}^{-1} = \dot{\mathbf{F}}_e \cdot \mathbf{F}_e^{-1} + \mathbf{F}_e \cdot \dot{\mathbf{F}}_{sl} \cdot \mathbf{F}_{sl}^{-1} \cdot \mathbf{F}_e^{-1} + \mathbf{F}_e \cdot \mathbf{F}_{sl} \cdot \dot{\mathbf{F}}_{tw} \cdot \mathbf{F}_{tw}^{-1} \cdot \mathbf{F}_{sl}^{-1} \cdot \mathbf{F}_e^{-1} = \mathbf{L}_e + \mathbf{L}_{sl} + \mathbf{L}_{tw}; \tag{5}$$

$$\mathbf{D} = \left(\dot{\mathbf{F}}_e \cdot \mathbf{F}_e^{-1}\right)_s + \left(\mathbf{F}_e \cdot \dot{\mathbf{F}}_{sl} \cdot \mathbf{F}_{sl}^{-1} \cdot \mathbf{F}_e^{-1}\right)_s + \left(\mathbf{F}_e \cdot \mathbf{F}_{sl} \cdot \dot{\mathbf{F}}_{tw} \cdot \mathbf{F}_{tw}^{-1} \cdot \mathbf{F}_{sl}^{-1} \cdot \mathbf{F}_e^{-1}\right)_s = \mathbf{D}_e + \mathbf{D}_{sl} + \mathbf{D}_{tw}. \tag{6}$$

The Green-Lagrange elastic strain tensor is used as the elastic strain measure yielding

$$\mathbf{E}_e = \frac{1}{2}\left(\mathbf{F}_e^T \cdot \mathbf{F}_e - \mathbf{I}\right) = \frac{1}{2}\left(\mathbf{U}_e \cdot \mathbf{U}_e - \mathbf{I}\right), \tag{7}$$

where $\mathbf{U}_e$ and $\mathbf{E}_e$ are defined in the configuration at the end of the plastic slip process. The relation between $\mathbf{D}_e = \left(\dot{\mathbf{F}}_e \cdot \mathbf{F}_e^{-1}\right)_s$ in Eq. (6) and the time rate of $\mathbf{E}_e$ can be obtained from the following (Levitas, 1996)

$$\begin{aligned} \left(\dot{\mathbf{F}}_e \cdot \mathbf{F}_e^{-1}\right)_s &= \frac{1}{2}\left(\dot{\mathbf{F}}_e \cdot \mathbf{F}_e^{-1} + \mathbf{F}_e^{-T} \cdot \dot{\mathbf{F}}_e^T\right) = \frac{1}{2}\mathbf{F}_e^{-T} \cdot \left(\mathbf{F}_e^T \cdot \dot{\mathbf{F}}_e + \dot{\mathbf{F}}_e^T \cdot \mathbf{F}_e\right) \cdot \mathbf{F}_e^{-1} \\ &= \frac{1}{2}\mathbf{F}_e^{-T} \cdot \left(\mathbf{F}_e^T \cdot \mathbf{F}_e\right)^{\bullet} \cdot \mathbf{F}_e^{-1} = \mathbf{F}_e^{-T} \cdot \left(\frac{1}{2}\left(\mathbf{F}_e^T \cdot \mathbf{F}_e - \mathbf{I}\right)\right)^{\bullet} \cdot \mathbf{F}_e^{-1} = \mathbf{F}_e^{-T} \cdot \dot{\mathbf{E}}_e \cdot \mathbf{F}_e^{-1}, \end{aligned} \tag{8}$$

where $(\ )^{\bullet}$ represents the time derivative for the expression in parenthesis.

Modelling of dislocation slip in multiphase materials is very sophisticated due to interactions among all slip modes in all twin variants or phases. As usual, we accept the kinematic relationship of Eq. (9), in which $\dot{\gamma}_{\beta i}$ is the plastic strain rate on slip system β of the *i*-th variant, the vector $\mathbf{s}_{\beta i}$ represents the slip direction, $\mathbf{m}_{\beta i}$ the slip plane normal, and the variant volumetric fraction is designated as c_i. In section 4, we will discuss how $\dot{\gamma}_{\beta i}$ linearly

depends on the mobile dislocation density $\rho_{M\beta i}$ for the slip system β of the *i*-th variant, and $\rho_{M\beta i}$ evolves by interaction with other dislocation systems of all variants.

$$\dot{\mathbf{F}}_{sl}\cdot\mathbf{F}_{sl}^{-1}=\sum_{i}\sum_{\beta}c_i\dot{\gamma}_{\beta i}\mathbf{s}_{\beta i}\otimes\mathbf{m}_{\beta i}\ . \tag{9}$$

In this paper, the subscripts α and β are used for slip systems, and the subscripts *i* and *j* for twin variants. Metals with an HCP crystal structure, are known to display prismatic $\langle a\rangle$, pyramidal $\langle a+c\rangle$ and basal slip. In the case of titanium, prismatic and pyramidal slip are predominant (Clouet et al., 2015; Nervo et al., 2016; Yoo et al., 2001), which are shown in Fig. 1 (a) and (b). There are fifteen slip systems total, α and β subscript designations used are 1-12 standing for the pyramidal slip systems, and 13-15 representing the prismatic systems. It is found that six tensile $\{10\bar{1}2\}\langle\bar{1}011\rangle$ and six compressive twin variants $\{11\bar{2}2\}\langle11\bar{2}\bar{3}\rangle$ are popular for zirconium/titanium single crystals (Beyerlein and Tomé, 2008; Morrow et al., 2016). The integer *i* or *j* varies from 0 to 12 and represents: parent material (number 0), six compressive twins (numbers 1-6) and six tensile twins (numbers 7-12).

For plastic velocity gradient due to twinning where twin variants are not explicitly represented topologically, it is commonly accepted that

$$\dot{\mathbf{F}}_{tw}\cdot\mathbf{F}_{tw}^{-1}=\sum_{i\,(i\neq0)}\dot{c}_i\gamma_{tw}\mathbf{b}_i\otimes\mathbf{n}_i\,, \tag{10}$$

where the scalar γ_{tw} is the constant twin variant shear magnitude when the parent material fully transforms into one variant $c_i=1$, the vector $\mathbf{b}_i$ represents the twinning direction and $\mathbf{n}_i$ the twin plane normal for the *i*-th twin. The summation $\sum_{i\,(i\neq0)}$ in Eq. (10) is with respect to all twinned variants not including the parent material $(i\neq0)$.

3. Application of thermodynamics laws

By combining the first (the energy balance equation) and second (the Clausius-Duhem inequality) laws of thermodynamics, we can obtain the dissipation rate in the local form (i.e. at any material point) defined in the current configuration:

$$\rho D = \boldsymbol{\sigma} : \mathbf{D} - \rho \dot{U} + \rho \dot{s} \theta - \frac{\nabla \theta}{\theta} \cdot \mathbf{h} \geq 0, \tag{11}$$

where $\boldsymbol{\sigma}$ is the Cauchy stress, U the specific internal energy (energy per unit mass), ρ the current density, temperature θ, heat flux vector $\mathbf{h}$, and entropy s. The detailed derivation of Eq. (11) can be found in a number of continuum mechanics textbooks (e.g. Clayton, 2010; Irgens, 2008). It is noted that the spatial gradient of the phase concentration rate contributes to Eq. (11) and this nonzero gradient is localized in nanoscale phase boundaries, which has been extensively studied by phase field simulations (e.g. Levitas and Warren, 2016). In this paper, because the titanium sample is millimeter size scale, we do not consider nanoscale theories. Consequently, the gradient term of phase concentration rate is dropped from the dissipation rate in Eq. (11), as in Feng and Levitas, (2017a,b) and other mesoscale/macroscale theories. As usual, it is accepted that the heat conduction described by the heat flux $\mathbf{h}$ and thermomechanical processes described by deformation state $\mathbf{D}$ and entropy rate $\dot{s}$ are mutually independent. Then the inequality Eq. (11) transforms to two well-known stronger inequalities in Eq. (12): Planck's inequality and Fourier's inequalities:

$$\rho D = \boldsymbol{\sigma} : \mathbf{D} - \rho \dot{U} + \rho \dot{s} \theta \geq 0; \qquad -\frac{\nabla \theta}{\theta} \cdot \mathbf{h} \geq 0. \tag{12}$$

Here, $-\frac{\nabla \theta}{\theta} \cdot \mathbf{h} \geq 0$ is automatically satisfied by all known experiments, and we use the same symbol D in the first equation of Eq. (12) with the one in Eq. (11). We introduce the specific Helmholtz free energy $\Psi(\mathbf{E}_e, \theta, c_1, ..., c_i, ..., c_n)$, in which the Green-Lagrange elastic strain $\mathbf{E}_e$ is defined in Eq. (7) and c_1 to c_n are the volume fractions of all *n* twinned variants. Here c_0 for the parent material is not included in Ψ, because there are only *n* independent volume fractions: $c_0 = 1 - \sum_{i=1}^{n} c_i$. Choosing any one of c_i excluded in Ψ is arbitrary, which does not make a difference in the final constitutive equations, and in this paper we exclude c_0 in Ψ. By using the specific Helmholtz free energy $\Psi = U - \theta s$, the dissipation rate in Eq. (12) yields

$$\rho D = \boldsymbol{\sigma} : \mathbf{D} - \rho \dot{\Psi} - \rho s \dot{\theta} \geq 0. \tag{13}$$

Combining Eqs. (6), (8) and (13), and sorting terms, we can further obtain

$$
\begin{aligned}
&\rho D=\boldsymbol{\sigma}:\left(\dot{\mathbf{F}}_e\cdot\mathbf{F}_e^{-1}+\mathbf{F}_e\cdot\dot{\mathbf{F}}_{sl}\cdot\mathbf{F}_{sl}^{-1}\cdot\mathbf{F}_e^{-1}+\mathbf{F}_e\cdot\mathbf{F}_{sl}\cdot\dot{\mathbf{F}}_{tw}\cdot\mathbf{F}_{tw}^{-1}\cdot\mathbf{F}_{sl}^{-1}\cdot\mathbf{F}_e^{-1}\right)-\rho\frac{\partial\Psi}{\partial\mathbf{E}_e}:\dot{\mathbf{E}}_e-\rho\frac{\partial\Psi}{\partial\theta}\dot{\theta}\\
&-\sum_{i=1}^{n}\rho\frac{\partial\Psi}{\partial c_i}\dot{c}_i-\rho s\dot{\theta}=\left(\boldsymbol{\sigma}:\dot{\mathbf{F}}_e\cdot\mathbf{F}_e^{-1}-\rho\frac{\partial\Psi}{\partial\mathbf{E}_e}:\dot{\mathbf{E}}_e\right)-\rho\left(\frac{\partial\Psi}{\partial\theta}+s\right)\dot{\theta}+\left(\boldsymbol{\sigma}:\mathbf{F}_e\cdot\dot{\mathbf{F}}_{sl}\cdot\mathbf{F}_{sl}^{-1}\cdot\mathbf{F}_e^{-1}\right)\\
&+\left(\boldsymbol{\sigma}:\mathbf{F}_e\cdot\mathbf{F}_{sl}\cdot\dot{\mathbf{F}}_{tw}\cdot\mathbf{F}_{tw}^{-1}\cdot\mathbf{F}_{sl}^{-1}\cdot\mathbf{F}_e^{-1}-\sum_{i=1}^{n}\rho\frac{\partial\Psi}{\partial c_i}\dot{c}_i\right)=\frac{\rho}{\tilde{\rho}}\left[\det\mathbf{F}_e\cdot\mathbf{F}_e^{-1}\cdot\boldsymbol{\sigma}\cdot\mathbf{F}_e^{-T}-\tilde{\rho}\frac{\partial\Psi}{\partial\mathbf{E}_e}\right]:\dot{\mathbf{E}}_e\\
&+\left(\boldsymbol{\sigma}:\mathbf{F}_e\cdot\mathbf{F}_{sl}\cdot\dot{\mathbf{F}}_{tw}\cdot\mathbf{F}_{tw}^{-1}\cdot\mathbf{F}_{sl}^{-1}\cdot\mathbf{F}_e^{-1}-\sum_{i=1}^{n}\rho\frac{\partial\Psi}{\partial c_i}\dot{c}_i\right)-\rho\left(\frac{\partial\Psi}{\partial\theta}+s\right)\dot{\theta}+\left[\boldsymbol{\sigma}:\mathbf{F}_e\cdot\dot{\mathbf{F}}_{sl}\cdot\mathbf{F}_{sl}^{-1}\cdot\mathbf{F}_e^{-1}\right]\geq 0
\end{aligned}
\tag{14}
$$

In Eq. (14), $\boldsymbol{\sigma}:\mathbf{D}=\boldsymbol{\sigma}:\mathbf{L}_s=\boldsymbol{\sigma}:\left(\mathbf{L}_s+\mathbf{L}_a\right)=\boldsymbol{\sigma}:\mathbf{L}$ is used, where the double contraction of symmetric with skew-symmetric tensors is zero. The quantity $\tilde{\rho}$ is the density at the intermediate configuration Ω_{sl} (at the end of plastic slip but before the current configuration). It is commonly accepted that the dissipation rate in Eq. (14) does not depend on elastic strain rate $\dot{\mathbf{E}}_e$ and temperature rate $\dot{\theta}$, we can obtain the elasticity rule in Eq. (15) and the entropy function in (16),

$$
\det\mathbf{F}_e\cdot\mathbf{F}_e^{-1}\cdot\boldsymbol{\sigma}\cdot\mathbf{F}_e^{-T}-\tilde{\rho}\frac{\partial\Psi}{\partial\mathbf{E}_e}=0\Rightarrow\boldsymbol{\sigma}=\frac{1}{\det\mathbf{F}_e}\mathbf{F}_e\cdot\tilde{\rho}\frac{\partial\Psi}{\partial\mathbf{E}_e}\cdot\mathbf{F}_e^{T},
\tag{15}
$$

$$
-\frac{\partial\Psi}{\partial\theta}=s.
\tag{16}
$$

When the viscoelasticity is considered and the elastic process is also dissipative, in addition to $\frac{1}{\det\mathbf{F}_e}\mathbf{F}_e\cdot\tilde{\rho}\frac{\partial\Psi}{\partial\mathbf{E}_e}\cdot\mathbf{F}_e^{T}$ in Eq. (15), the Cauchy stress also depends on the strain rate $\dot{\mathbf{G}}_e=\frac{1}{\det\mathbf{F}_e}\mathbf{F}_e\cdot\dot{\mathbf{E}}_e\cdot\mathbf{F}_e^{T}$. Consequently, Eq. (15) becomes

$$
\boldsymbol{\sigma}=\frac{1}{\det\mathbf{F}_e}\mathbf{F}_e\cdot\tilde{\rho}\frac{\partial\Psi}{\partial\mathbf{E}_e}\cdot\mathbf{F}_e^{T}+f\left(\dot{\mathbf{G}}_e\right).
\tag{17}
$$

In viscoelasticity, many times it is assumed that $f\left(\dot{\mathbf{G}}_e\right)$ linearly depends on $\dot{\mathbf{G}}_e$ as $f\left(\dot{\mathbf{G}}_e\right)=\mathbf{K}:\dot{\mathbf{G}}_e$, where $\mathbf{K}$ is the fourth-rank viscosity tensor. To satisfy the dissipation inequality for elasticity process, $\dot{\mathbf{G}}_e:\mathbf{K}:\dot{\mathbf{G}}_e\geq 0$, which indicates the viscosity tensor $\mathbf{K}$ is a positive semi-definite tensor. In this paper, due to lack of information on $\mathbf{K}$ and as is the case of

models under high strain loadings (e.g. Luscher et al., 2017), we only consider viscoplasticity and ignore the time dependence in the elasticity. This assumption is also reasonable because elastic deformation and elastic strain rate in the current simulation are very small and the stress only reaches 500 MPa for the titanium experiments considered in this work.

Combining Eqs. (15) and (16) with Eq. (14), the dissipation rate due to plastic slip and twinning yields,

$$\boldsymbol{\sigma}:\mathbf{F}_e\cdot\dot{\mathbf{F}}_{sl}\cdot\mathbf{F}_{sl}^{-1}\cdot\mathbf{F}_e^{-1}+\left(\boldsymbol{\sigma}:\mathbf{F}_e\cdot\mathbf{F}_{sl}\cdot\dot{\mathbf{F}}_{tw}\cdot\mathbf{F}_{tw}^{-1}\cdot\mathbf{F}_{sl}^{-1}\cdot\mathbf{F}_e^{-1}-\sum_{i=1}^{n}\rho\frac{\partial\Psi}{\partial c_i}\dot{c}_i\right)\geq 0 \tag{18}$$

Since both twinning and slip processes in Eq. (18) are dissipative processes (i.e. entropy increases during each of the processes), and therefore both terms in Eq. (18) must be non-negative. This leads to two separate inequalities: Eqs. (19) and (20). For dislocation slip, we have

$$\begin{aligned}&\boldsymbol{\sigma}:\mathbf{F}_e\cdot\dot{\mathbf{F}}_{sl}\cdot\mathbf{F}_{sl}^{-1}\cdot\mathbf{F}_e^{-1}=\mathbf{F}_e^{-1}\cdot\boldsymbol{\sigma}\cdot\mathbf{F}_e:\dot{\mathbf{F}}_{sl}\cdot\mathbf{F}_{sl}^{-1}=\mathbf{F}_e^{-1}\cdot\boldsymbol{\sigma}\cdot\mathbf{F}_e:\left(\sum_i\sum_\beta c_i\dot{\gamma}_{\beta i}\mathbf{s}_{\beta i}\otimes\mathbf{m}_{\beta i}\right)\\&=\sum_i\sum_\beta c_i\left[\mathbf{F}_e^{-1}\cdot\boldsymbol{\sigma}\cdot\mathbf{F}_e:\left(\mathbf{s}_{\beta i}\otimes\mathbf{m}_{\beta i}\right)\right]\dot{\gamma}_{\beta i}\geq 0.\end{aligned} \tag{19}$$

To satisfy the inequality of Eq. (19) and the non-negative dissipation for each slip system of each variant, the $\mathbf{F}_e^{-1}\cdot\boldsymbol{\sigma}\cdot\mathbf{F}_e:\left(\mathbf{s}_{\beta i}\otimes\mathbf{m}_{\beta i}\right)$ and $\dot{\gamma}_{\beta i}$ should always have the same sign, which indicates that $\dot{\gamma}_{\beta i}$ has to be a direct function of $\tau_{\beta i}$,

$$\tau_{\beta i}=\mathbf{F}_e^{-1}\cdot\boldsymbol{\sigma}\cdot\mathbf{F}_e:\left(\mathbf{s}_{\beta i}\otimes\mathbf{m}_{\beta i}\right). \tag{20}$$

This $\tau_{\beta i}$ is the driving force for plastic slip on system β in the *i*-th variant (*i* can be any variant including the parent material (*i* =0)). In literature, the resolved shear stress for plastic slip $\dot{\gamma}_{\beta i}$ can be defined differently from $\tau_{\beta i}$ in Eq. (20). In literature, the resolved shear stress is obtained by double contraction between the Schmid tensor and stress tensors such as the Cauchy stress tensor (e.g. in Sun et al., (2016)), second Piola-Kirchhoff stress (e.g. in Salem et al., (2005)), or the Kirchhoff stress (e.g. in Abdolvand et al., (2011)), which are not a direct function of Eq. (20). In this paper, by using resolved shear stress $\tau_{\beta i}=\mathbf{F}_e^{-1}\cdot\boldsymbol{\sigma}\cdot\mathbf{F}_e:\left(\mathbf{s}_{\beta i}\otimes\mathbf{m}_{\beta i}\right)$, it allows the plastic slip to always be dissipative, which is thermodynamically consistent. Specifically, the sign of $\dot{\gamma}_{\beta i}$ is

determined by the sign of dislocation velocity (see Eq. (49)), and the sign of dislocation velocity is always consistent with the sign of $\tau_{\beta i}$ (see Eq. (31)). Therefore, $c_i\left[\mathbf{F}_e^{-1}\cdot\boldsymbol{\sigma}\cdot\mathbf{F}_e:\left(\mathbf{s}_{\beta i}\otimes\mathbf{m}_{\beta i}\right)\right]\dot{\gamma}_{\beta i}=c_i\tau_{\beta i}\dot{\gamma}_{\beta i}\geq 0$ is always satisfied in our model. It is noted that in crystal plasticity theories with absence of twinning, it is common to find the expression $\tau_{\beta 0}=\boldsymbol{\sigma}:\left(\mathbf{F}_e\cdot\mathbf{s}_{\beta 0}\otimes\mathbf{m}_{\beta 0}\cdot\mathbf{F}_e^{-1}\right)$ in literature (i.e. (Khan and Huang, 1995; Asaro, 1983)), which is consistent with our resolved shear stress for slip. When twinning is considered, $\mathbf{s}_{\beta i}\otimes\mathbf{m}_{\beta i}$ in the resolved shear stress is deformed by the elastic deformation gradient and rotated with the rule in Eq. (30) and (56) if Cauchy stress or Kirchhoff stress is used for resolved shear stress. It is rare (if there is any) to see the expression in Eq. (20) in literature and the deformation of $\mathbf{s}_{\beta i}\otimes\mathbf{m}_{\beta i}$ is frequently ignored.

For the plastic twinning process, we have the following inequality:

$$\begin{aligned}&\boldsymbol{\sigma}:\mathbf{F}_e\cdot\mathbf{F}_{sl}\cdot\dot{\mathbf{F}}_{tw}\cdot\mathbf{F}_{tw}^{-1}\cdot\mathbf{F}_{sl}^{-1}\cdot\mathbf{F}_e^{-1}-\sum_{i=1}^{n}\rho\frac{\partial\Psi}{\partial c_i}\dot{c}_i=\mathbf{F}_{sl}^{-1}\cdot\mathbf{F}_e^{-1}\cdot\boldsymbol{\sigma}\cdot\mathbf{F}_e\cdot\mathbf{F}_{sl}:\dot{\mathbf{F}}_{tw}\cdot\mathbf{F}_{tw}^{-1}-\sum_{i=1}^{n}\rho\frac{\partial\Psi}{\partial c_i}\dot{c}_i\\&=\sum_{i=1}^{n}\mathbf{F}_{sl}^{-1}\cdot\mathbf{F}_e^{-1}\cdot\boldsymbol{\sigma}\cdot\mathbf{F}_e\cdot\mathbf{F}_{sl}:\mathbf{b}_i\otimes\mathbf{n}_i\dot{c}_i\gamma_{tw}-\sum_{i=1}^{n}\rho\frac{\partial\Psi}{\partial c_i}\dot{c}_i\geq 0.\end{aligned}\tag{21}$$

For the titanium material used in this work under SHPB loading conditions,

$$\sum_{i=1}^{n}\mathbf{F}_{sl}^{-1}\cdot\mathbf{F}_e^{-1}\cdot\boldsymbol{\sigma}\cdot\mathbf{F}_e\cdot\mathbf{F}_{sl}:\mathbf{b}_i\otimes\mathbf{n}_i\dot{c}_i>>\frac{1}{\gamma_{tw}}\sum_{i=1}^{n}\rho\frac{\partial\Psi}{\partial c_i}\dot{c}_i,\tag{22}$$

in which $\sum_{i=1}^{n}$ is the summation for all of *n* twinned variants but does not include the parent material (*i*=0). The effect of $\sum_{i=1}^{n}\rho\frac{\partial\Psi}{\partial c_i}\dot{c}_i$ in the inequality of Eq. (21) can be ignored (i.e. Eq. (22)) for two reasons: first the rotation of the elastic stiffness matrix due to twinning is small, and second the elastic strain is much less than twinning strain (See details in Section 4). The dimensional analysis presented below will demonstrate this. Thus, we have

$$\sum_{i=1}^{n}\mathbf{F}_{sl}^{-1}\cdot\mathbf{F}_e^{-1}\cdot\boldsymbol{\sigma}\cdot\mathbf{F}_e\cdot\mathbf{F}_{sl}:\mathbf{b}_i\otimes\mathbf{n}_i\dot{c}_i\gamma_{tw}=\sum_{i=1}^{n}\tau_{tw-i}\dot{c}_i\gamma_{tw}\geq 0;\quad \tau_{tw-i}=\mathbf{F}_{sl}^{-1}\cdot\mathbf{F}_e^{-1}\cdot\boldsymbol{\sigma}\cdot\mathbf{F}_e\cdot\mathbf{F}_{sl}:\mathbf{b}_i\otimes\mathbf{n}_i.\tag{23}$$

The driving force for the *i*-th twin variant is τ_{tw-i} in Eq. (23), and $\dot{c}_i$ must be a function of τ_{tw-i} to satisfy this inequality for each twinning process, since γ_{tw} is a positive material constant and

does not affect the sign. However, there are many different definitions in literature for the resolved shear stress τ_{tw-i} for twinning, which are not the same as that defined in Eq. (23) and not thermodynamically admissible at large strains. For example, in Salem et al., (2005) the positive sign of $\dot{c}_i$ is assured by the resolved shear stress as $\tau = \mathbf{T}:\mathbf{b}_i \otimes \mathbf{n}_i > 0$ ($\mathbf{T}$ is the second Piola-Kirchhoff stress defined in Eq. (27))). In large deformation, $\mathbf{T}:\mathbf{b}_i \otimes \mathbf{n}_i$ (or other resolved shear stresses in literature) and $\tau_{tw-i} = \mathbf{F}_{sl}^{-1}\cdot\mathbf{F}_e^{-1}\cdot\boldsymbol{\sigma}\cdot\mathbf{F}_e\cdot\mathbf{F}_{sl}:\mathbf{b}_i \otimes \mathbf{n}_i$ in Eq. (23) can be quite different, and one can always apply the load in a way having $\mathbf{T}:\mathbf{b}_i \otimes \mathbf{n}_i > 0$ and $\mathbf{F}_{sl}^{-1}\cdot\mathbf{F}_e^{-1}\cdot\boldsymbol{\sigma}\cdot\mathbf{F}_e\cdot\mathbf{F}_{sl}:\mathbf{b}_i \otimes \mathbf{n}_i < 0$, which does not obey the second law of thermodynamics in Eq. (23). Without $\mathbf{F}_p = \mathbf{F}_{sl}\cdot\mathbf{F}_{tw}$ or $\mathbf{F}_p = \mathbf{F}_{tw}\cdot\mathbf{F}_{sl}$, the resolved shear stress for either plastic slip or twinning may not be obtained to be strictly satisfied by the second law of thermodynamics in Eq. (13).

4. Constitutive relations and material parameters

4.1 Elasticity rule.

Helmholtz free energy $\Psi(\mathbf{E}_e, c_1, ..., c_n)$ is considered as a function of the Green-Lagrange elastic strain tensor $\mathbf{E}_e$ and concentrations of the twin variants. For a small elastic deformation as considered here, it can be taken that

$$\tilde{\rho}\Psi = \frac{1}{2}\mathbf{E}_e:\mathbf{C}:\mathbf{E}_e = \frac{1}{2}\mathbf{E}_e:\sum_{i=0}^{n} c_i\mathbf{C}_i:\mathbf{E}_e, \qquad c_0 = 1-\sum_{i=1}^{n} c_i \tag{24}$$

where $\tilde{\rho}$ is the density in the intermediate configuration Ω_{sl} and $\mathbf{C}$ is the fourth-order elastic stiffness tensor, which is a function of the volume fraction c_i of each variant and the elastic stiffness of each variant $\mathbf{C}_i$ as $\mathbf{C} = \sum_i c_i\mathbf{C}_i$. For high-order-strain constitutive behavior with larger elastic deformation, $\mathbf{C}_i$ can be a function of the elastic strain tensor. For example, under megabar pressure, the high-order elastic strain theory for cubic diamond is considered in Feng and Levitas (2017b) and Feng et al. (2016). Lattice rotations of the twinned region relative to the untwinned crystal can be introduced by a rotation tensor $\mathbf{R}_i$ (Kalidindi, 1998),

$$\mathbf{R}_i = 2\mathbf{n}_i \otimes \mathbf{n}_i - \mathbf{I}. \tag{25}$$

Here unit vector $\mathbf{n}_i$ is the twin plane normal of the *i*-th twin variant.

Let the elastic stiffness tensor for untwinned material $\mathbf{C}_0$ be written as $\mathbf{C}_0 = C_{0-lmjk}\mathbf{e}_l\mathbf{e}_m\mathbf{e}_j\mathbf{e}_k$ in the base $\mathbf{e}_l\mathbf{e}_m\mathbf{e}_j\mathbf{e}_k$. Further, the stiffness $\mathbf{C}_i$ for the *i*-th twin (Kalidindi, 1998) can be obtained from

$$\mathbf{C}_i = C_{0-lmjk}\left(\mathbf{R}_i\cdot\mathbf{e}_l\right)\left(\mathbf{R}_i\cdot\mathbf{e}_m\right)\left(\mathbf{R}_i\cdot\mathbf{e}_j\right)\left(\mathbf{R}_i\cdot\mathbf{e}_k\right). \tag{26}$$

Combining the elasticity rule in Eq. (15) and free energy function in Eq. (24), we have the Cauchy stress in the current configuration Ω and the second Piola-Kirchhoff stress $\mathbf{T}$ in the Ω_{sl} configuration yielding

$$\boldsymbol{\sigma} = \frac{1}{\det\mathbf{F}_e}\mathbf{F}_e\cdot\tilde{\rho}\frac{\partial\Psi}{\partial\mathbf{E}_e}\cdot\mathbf{F}_e^T = \frac{1}{\det\mathbf{F}_e}\mathbf{F}_e\cdot\left(\mathbf{C}:\mathbf{E}_e\right)\cdot\mathbf{F}_e^T = \frac{1}{\det\mathbf{F}_e}\mathbf{F}_e\cdot\mathbf{T}\cdot\mathbf{F}_e^T, \tag{27}$$

where $\mathbf{T} = \tilde{\rho}\dfrac{\partial\Psi}{\partial\mathbf{E}_e} = \mathbf{C}:\mathbf{E}_e$.

Let us evaluate the approximate magnitude of the right hand side of Eq. (22) from Eq. (24), we have

$$\frac{1}{\gamma_{tw}}\sum_{i=1}^{n}\rho\frac{\partial\Psi}{\partial c_i}\dot{c}_i = \frac{1}{2}\frac{\rho}{\tilde{\rho}}\sum_{i=1}^{n}\frac{\mathbf{E}_e}{\gamma_{tw}}:\left(\mathbf{C}_i-\mathbf{C}_0\right):\mathbf{E}_e\dot{c}_i \simeq \frac{1}{2}\sum_{i=1}^{n}\frac{\mathbf{E}_e}{\gamma_{tw}}:\left(\mathbf{C}_i-\mathbf{C}_0\right):\mathbf{E}_e\dot{c}_i, \tag{28}$$

In our model, the elastic volumetric strain under SHPB is very small since the pressure is only a few hundred MPa and thus $\dfrac{\rho}{\tilde{\rho}}\simeq 1$ is used in Eq. (28). During rotation, the changes in components of $\mathbf{C}_i$ from $\mathbf{C}_0$ may be small, and thus $\mathbf{C}\simeq\mathbf{C}_i\simeq\mathbf{C}_0$. Specifically, Table 1 exhibits the elastic constants of the HCP titanium (Fisher and Renken, 1964; Vohra, 1978). If C_{33} is reduced by 7%, the elastic behavior of titanium is equivalent to the cubic lattice with three elastic constants C_{11}, C_{12} and C_{44}. Further, $2C_{44}/\left(C_{11}-C_{12}\right)=1.037$, which is very close to 1.0 for isotropic materials. In addition, our results in simulations show that the normal elastic strain component is around 1% of $\gamma_{tw}=0.2$. In Eq. (28), both $\dfrac{\mathbf{E}_e}{\gamma_{tw}}$ and $\left(\mathbf{C}_i-\mathbf{C}_0\right)$ cause that the value of $\dfrac{1}{\gamma_{tw}}\sum_{i=1}^{n}\rho\dfrac{\partial\Psi}{\partial c_i}\dot{c}_i$ is much smaller than the left hand side of Eq. (22):

$$\sum_{i=1}^{n}\mathbf{F}_{sl}^{-T}\cdot\mathbf{F}_e^{-T}\cdot\boldsymbol{\sigma}\cdot\mathbf{F}_e\cdot\mathbf{F}_{sl}:\mathbf{b}_i\otimes\mathbf{n}_i\dot{c}_i \simeq \sum_{i=1}^{n}\boldsymbol{\sigma}:\mathbf{b}_i\otimes\mathbf{n}_i\dot{c}_i \simeq \sum_{i=1}^{n}\mathbf{C}:\mathbf{E}_e:\mathbf{b}_i\otimes\mathbf{n}_i\dot{c}_i. \tag{29}$$

Here $\mathbf{b}_i \otimes \mathbf{n}_i$ is not small in comparison with the unit tensor since the rotation is large but $\frac{\mathbf{E}_e}{\gamma_{tw}}$ is small. Our simulation results on titanium under SHPB show that Eq. (29) is approximately three orders of magnitude larger than Eq. (28).

Elastic constants	C_{11}, C_{22}	C_{33} (*c* axis)	C_{12}, C_{13}, C_{23}	C_{44}, C_{55}, C_{66}
Magnitude (GPa)	177.59	191.34	87.57	46.7

Table 1: Elastic stiffness for the HCP titanium (Fisher and Renken, 1964; Vohra, 1978).

4.2 Dislocation-based crystal plasticity in heterogeneous materials.

Thermodynamically consistent dislocation based viscoplasticity will be introduced in this section. While we focus on modeling of plastic slip in parent HCP titanium and twin variants, the model can be applied to the heterogeneous materials of multiple phases and compositions. As mentioned earlier, fifteen slip systems are most often considered for single crystal HCP titanium, including twelve pyramidal and three prismatic. Since crystallographic reorientation occurs within twinned regions, each twin also has fifteen slip systems. The orientation of the Schmid tensor for slip is rotated together with the rotation of the crystal lattice by the following rule (Kalidindi, 1998):

$$\mathbf{s}_{\beta i} \otimes \mathbf{m}_{\beta i} = \mathbf{R}_i \cdot \left(\mathbf{s}_{\beta 0} \otimes \mathbf{m}_{\beta 0} \right) \cdot \mathbf{R}_i^T , \tag{30}$$

where the rotation tensor $\mathbf{R}_i$ is from Eq. (25) and $\mathbf{s}_{\beta 0} \otimes \mathbf{m}_{\beta 0}$ is the Schmid tensor of the parent material. Let us consider the representative volume *V* consisting of a mixture of *m* twin variants. We further divide *V* into *m* districts, where the volume of each district is $c_i V$, and one district stands for one variant only. In the *i*-th district, the dislocation density is ρ_i which does not consider the size of this district compared to the entire *V*, and the dislocation density within the *i*-th variant in this *V* is $N_i = c_i \rho_i$. We do not isolate each district but do consider the interactions of all slip systems of all variants in this *V*. In this paper, when we use the symbol ρ_i, we refer to the dislocation density within a district, and N_i is used for dislocation density directly in *V*. An advanced theory is proposed in this paper based on the single crystal plasticity theory in Hansen et al. (2013) and now applied to the multiphase or multi-variant materials and the interactions among dislocations in different slip systems more generally.

We hypothesize that dislocations fall into three classes of populations and are thereby formulated as such in this work: (1) mobile dislocations (*M*) which is the only population having appreciable velocity in a material, (2) pileup dislocations (*P*) which are generated by the pileup of mobile dislocations and can become mobile if they escape from the temporary sessile state, and (3) locked sessile dislocations (*L*) which do not belong to any slip system and are generated when the mobile dislocations form locks and become sessile.

The average mobile dislocation velocity is accepted (e.g. Luscher et al., 2017):

$$v_{\alpha i} = \frac{\tau_{\alpha i} b_{\alpha i}}{B_{\alpha i}}, \tag{31}$$

where $b_{\alpha i}$ is the magnitude of the Burgers vector at the slip mode α of the *i*-th variant, $\tau_{\alpha i}$ is the resolved shear stress for plastic slip (see its definition in Eq. (20)) which is the only term in Eq. (31) determining the sign of $v_{\alpha i}$ as positive, negative or zero, and $B_{\alpha i}$ is the viscous drag coefficient that increases without bound as $v_{\alpha i}$ approaches the shear wave speed, c_s, according to

$$B_{\alpha i} = \frac{B_0}{1-\left(v_{\alpha i}/c_s\right)^2}, \tag{32}$$

where the constant B_0 is the nominal value of the damping coefficient. The damping effect is trivial in titanium under SHPB since c_s is around 6000 m/s which is a factor of 20 higher in comparison to the dislocation velocities obtained from our simulations in Section 5. Consequently we can directly use B_0 for $B_{\alpha i}$ in our simulations.

4.2.1 Dislocation interactions

Let us consider the interaction of dislocations on two slip systems $N_{A\alpha i}$ and $N_{B\beta j}$, where the subscripts *A* and *B* represent the dislocation types (*M* or *P*), α and β stand for slip systems, and *i* and *j* are for the different twin variants. From Hansen et al. (2013), the time rate of change of dislocation density $N_{A\alpha i}$ of type *A* in the slip system α of the *i*-th variant during the interaction with $N_{B\beta j}$ can be written as

$$\dot{N}^{inter}_{A\alpha i-B\beta j} = P^{inter}_{A\alpha i-B\beta j} D^{inter}_{A\alpha i-B\beta j} f^{inter}_{A\alpha i-B\beta j} N_{A\alpha i} N_{B\beta j} \left| \boldsymbol{v}_{A\alpha i-B\beta j} \right|. \quad (33)$$

The rate $\dot{N}^{inter}_{A\alpha i-B\beta j}$ indicates that under such states of mean relative dislocation velocity $\boldsymbol{v}_{A\alpha i-B\beta j}$ the dislocation density $N_{A\alpha i}$ changes from one type into a different type such as from mobile to locked sessile dislocations. In Eq. (33) $D^{inter}_{A\alpha i-B\beta j}$ is the interaction distance under which the interactions between $N_{A\alpha i}$ and $N_{B\beta j}$ can take place, and $\left| \boldsymbol{v}_{A\alpha i-B\beta j} \right|$ is the magnitude of the relative velocity of dislocations of these two different types. The term $f^{inter}_{A\alpha i-B\beta j}$ is the fraction of dislocation density $N_{A\alpha i}$ having interactions and changing the dislocation type. Annihilation must occur between two dislocations with opposite Burgers vectors, and thus they mostly occur in the same slip systems (annihilation may also occur in the collinear slip systems but the possibility is much rarer). We assume that an equal proportion of edge and screw character dislocations on all slip systems and half of the dislocations having the opposite Burgers vector and the other half have the same Burgers vector in either screw or edge dislocations. A fraction of ¼ is used for both annihilation and pileup when they occur in $N_{A\alpha i}$ only (i.e. when $N_{A\alpha i}$ does not annihilate with or pile up on $N_{B\beta j}$). When $N_{A\alpha i}$ annihilates with or piles up on $N_{B\beta j}$, $f^{annil}_{A\alpha i-B\beta j} < ¼$ when $N_{B\beta j} < N_{A\alpha i}$ (because when $N_{A\alpha i}$ is ready to annihilate or pile up it is assumed that there are not enough $N_{B\beta j}$ to let them do so) but the fraction is still ¼ when $N_{B\beta j} \geq N_{A\alpha i}$. In addition to dislocation pileup and annihilation, there are other actions during interactions: pileup dislocations escape and become mobile again; mobile dislocations can form a sessile lock with mobile or pileup dislocations. The sessile locks are assumed to form at a fraction $f^{L}_{A\alpha i-B\beta j}$. All slip systems will be treated as equally likely to free a pileup dislocation, and thus for the escape of $N_{P\alpha i}$, $f^{esc}_{P\alpha i-M\beta j} = f^{esc}$, and pileup dislocations $N_{P\alpha i}$ cannot escape by interacting with $N_{P\beta j}$ due to zero relative velocity between these two slip systems. $N_{P\alpha i}$ must interact with a mobile dislocation $N_{M\beta j}$ to escape. In Eq. (33), the thermal probability $P^{inter}_{A\alpha i}$ is recognized as the thermal barrier for the occurrence of an interaction. Attraction exists between dislocations with opposite Burgers vector and annihilation always minimizes local energy, which leads to reduction of

energy and $P_{A\alpha i}^{Anni}=1$. Thermal probability of forming a sessile lock is also unity due to minimizing energy as well. The escape of pileup dislocations and the trap of dislocations for pileup are considered as thermal processes governed by an Arrhenius equation

$$P_{A\alpha i}^{esc}=e^{esc}=\exp\left(\frac{\left(\left(\tau_{\alpha i}^{G}-\left|\tau_{\alpha i}\right|\right)b_{\alpha i}{}^{2}-K_{Aai}\right)L}{-k_b\theta}\right);\ P_{A\alpha i}^{trap}=e^{-esc}=\exp\left(\frac{\left(\left(\tau_{\alpha i}^{G}-\left|\tau_{\alpha i}\right|\right)b_{\alpha i}{}^{2}-K_{Aai}\right)L}{k_b\theta}\right),\quad (34)$$

where $\tau_{\alpha i}^{G}b_{\alpha i}$ is the average force per unit length for overcoming a barrier to dislocation motion on slip system α for the *i*-th variant; k_b and θ are the Boltzmann's constant and temperature, respectively; *L* is the average distance over which forces $\tau_{\alpha i}b_{\alpha i}$ act to overcome an obstacle; the average kinetic energy K_{Aai} is defined as $K_{Aai}=\frac{1}{2}mv_{Aai}^{2}$, where *m* is the effective dislocation line mass. It is noted that the probability of dislocations to pile-up or escape is limited to 1. For example, when the sign of *esc* in Eq. (34) becomes positive the probability is set as unity for $P_{A\alpha i}^{esc}$. The resistance to dislocation motion $\tau_{\alpha i}^{G}$ is defined as

$$\tau_{\alpha i}^{G}=k_1\mu b_{\alpha i}\sqrt{N_{\alpha i}^{I}}+\tau_0^{\alpha,i},\quad (35)$$

where $\tau_0^{\alpha,i}$ is the intrinsic lattice resistance or Peierls stress, and $N_{\alpha i}^{I}$ is the dislocation impediment density for the α slip system of the *i*-th variant, which is defined from Cuitino and Ortiz (1993) as

$$N_{\alpha i}^{I}=\left(\frac{2}{\pi}\right)^{2}N^{L}+\sum_{j}\sum_{\beta}\frac{2}{\pi}\sqrt{1-\left(\mathbf{n}_{\alpha i}\cdot\mathbf{n}_{\beta j}\right)^{2}}\left(N_{M\beta j}+N_{P\beta j}\right),\quad (36)$$

where N^{L} is the locked dislocation density. Note that the total rate of change for a specific dislocation type $N_{A\alpha i}$ during all interactions can be written as

$$\dot{N}_{A\alpha i}^{inter}=\sum_{B}\sum_{\beta}\sum_{j}\dot{N}_{A\alpha i-B\beta j}^{inter}\ .\quad (37)$$

4.2.2 Dislocation density evolution

Mobile dislocation density is the only type that has a nonzero velocity and thus when the interaction between two slip systems occurs, the mobile velocity on at least one of the systems must be non-zero for change to occur. During the interaction with dislocation density $N_{B\beta j}$,

mobile dislocation density $N_{M\alpha i}$ can pile up $\dot{N}^{pile-Mai}_{M\alpha i-B\beta j}$, annihilate $\dot{N}^{anni-Mai}_{M\alpha i-B\beta j}$ or form sessile locks $\dot{N}^{lock-Mai}_{M\alpha i-B\beta j}$:

$$\dot{N}^{inter}_{M\alpha i}=\sum_B\sum_\beta\sum_j \dot{N}^{inter}_{M\alpha i-B\beta j}=\sum_B\sum_\beta\sum_j \dot{N}^{lock-Mai}_{M\alpha i-B\beta j}+\sum_B\sum_\beta\sum_j \dot{N}^{pile-Mai}_{M\alpha i-B\beta j}+\sum_B\sum_\beta\sum_j \dot{N}^{anni-Mai}_{M\alpha i-B\beta j}, \quad (38)$$

where $\dot{N}^{inter}_{M\alpha i}$ is the total rate of change of mobile dislocation density $N_{M\alpha i}$ during interactions. Based on the simple volume fraction mixing relationship $N_{A\alpha i}=c_i\rho_{A\alpha i}$, we have

$$\dot{N}^{inter}_{A\alpha i}=c_i\dot{\rho}^{inter}_{A\alpha i}+\dot{c}_i\rho^{inter}_{A\alpha i}=c_i\dot{\rho}^{inter}_{A\alpha i}, \quad (39)$$

in which plastic-slip-induced twinning is not considered, and c_i remains constant during the plastic slip process over a time step (i.e. $\dot{c}_i=0$). Consequently, Eqs. (33) and (38) transform into

$$\dot{\rho}^{inter}_{A\alpha i}=\sum_B\sum_\beta\sum_j P^{inter}_{A\alpha i-B\beta j}D^{inter}_{A\alpha i-B\beta j}f^{inter}_{A\alpha i-B\beta j}\rho_{A\alpha i}N_{B\beta j}\left|v_{A\alpha i-B\beta j}\right|, \quad (40)$$

$$\dot{\rho}^{inter}_{M\alpha i}=\sum_B\sum_\beta\sum_j \dot{\rho}^{lock}_{M\alpha i-B\beta j}+\sum_B\sum_\beta\sum_j \dot{\rho}^{pile-Mai}_{M\alpha i-B\beta j}+\sum_B\sum_\beta\sum_j \dot{\rho}^{anni-Mai}_{M\alpha i-B\beta j}. \quad (41)$$

The dislocation density $\dot{\rho}^{inter}_{M\alpha i}$ rather than $\dot{N}^{inter}_{A\alpha i}$ is updated at any local point and time. Such a treatment indicates that if a twin variant with a concentration close to zero does not affect the dislocation density in other variants but $\rho_{M\alpha i}$ of this variant ($N_{M\alpha i}$ still close to zero) can be affected by other variants significantly. When the dislocation pileup and annihilation are considered, one of the differences in this paper from Hansen et al. 2013 is that we distinguish the interaction between the two different slip systems and the same slip systems. When the slip system $B\beta j\ (\beta j\neq\alpha i)$ causes the pileup and annihilation of $M\alpha i$, the pileup and annihilation take places among $M\alpha i$. However, when $B\beta j=P\alpha i$, there are two different cases: the pileup and annihilation of $M\alpha i$ can occur in itself $M\alpha i$ (by using symbol $\dot{\rho}^{pile-itself}_{M\alpha i-P\alpha i}$ and $\dot{\rho}^{anni-itself}_{M\alpha i-P\alpha i}$), or pile up and annihilate with $P\alpha i$ ($\dot{\rho}^{pile-MP}_{M\alpha i-P\alpha i}$ and $\dot{\rho}^{anni-MP}_{M\alpha i-P\alpha i}$).

Further we have

$$\begin{aligned}\sum_B\sum_\beta\sum_j \dot{\rho}^{pile-Mai}_{M\alpha i-B\beta j}&=\sum_B\sum_\beta\sum_j \dot{\rho}^{pile-itself}_{M\alpha i-B\beta j}+\dot{\rho}^{pile-MP}_{M\alpha i-P\alpha i}\\&=\sum_B\sum_\beta\sum_j P^{trap}_{Mai}D^{pile\text{-}itself}_{M\alpha i-B\beta j}f^{pile-itself}_{M\alpha i-B\beta j}\rho_{M\alpha i}c_j\rho_{B\beta j}\left|v_{M\alpha i-B\beta j}\right|+P^{trap}_{Mai}D^{pile\text{-}MP}_{M\alpha i-P\alpha i}f^{pile\text{-}MP}_{M\alpha i-P\alpha i}\rho_{M\alpha i}c_i\rho_{P\alpha i}\left|v_{M\alpha i}\right|\end{aligned} \quad (42)$$

$$\sum_B \sum_\beta \sum_j \dot{\rho}^{anni-M\alpha i}_{M\alpha i-B\beta j} = \sum_B \sum_\beta \sum_j \dot{\rho}^{anni-itself}_{M\alpha i-B\beta j} + \dot{\rho}^{anni-MP}_{M\alpha i-P\alpha i}$$
$$= \sum_B \sum_i \sum_j D^{anni\text{-}itself}_{M\alpha i-B\beta j} f^{anni-itself}_{M\alpha i-B\beta j} \rho_{M\alpha i} c_j \rho_{B\beta j} \left| v_{M\alpha i-B\beta j} \right| + D^{anni\text{-}MP}_{M\alpha i-P\alpha i} f^{anni\text{-}MP}_{M\alpha i-P\alpha i} \rho_{M\alpha i} c_i \rho_{P\alpha i} \left| v_{M\alpha i} \right| \quad . \tag{43}$$

In addition to mobile dislocation density $N_{M\alpha i}$ interacting with others causing the population change, there are several sources resulting in its increase, which includes homogeneous nucleation $\dot{\rho}^{gen}_{M\alpha i}$, the propagation of mobile dislocations from a set of dislocation sources $\dot{\rho}^{prop}_{M\alpha i}$, and the escape of pileup dislocations $\dot{\rho}^{esc}_{P\alpha i}$. Here, we update the dislocation density $\rho_{M\alpha i}$ instead of $N_{M\alpha i}$ as well. The total rate in mobile dislocation density in the slip system α of the *i*-th phase

$$\dot{\rho}_{M\alpha i} = \dot{\rho}^{gen}_{M\alpha i} + \dot{\rho}^{prop}_{M\alpha i} + \dot{\rho}^{esc}_{P\alpha i} - \dot{\rho}^{inter}_{M\alpha i} \, . \tag{44}$$

Homogeneous nucleation of dislocations $\dot{\rho}^{gen}_{M\alpha i}$ occurs within a perfect lattice, which requires a very large external stress or thermal fluctuations. It is only considered in the theoretical development in Eq. (44), and for the application to the SHPB experiments we do not include this term because of the relatively low levels of stress achieved, as the same treatments in (Hansen, et al. 2013; Luscher et al., 2017). The propagation term $\dot{\rho}^{prop}_{M\alpha i}$ is the dislocation nucleation based on existing dislocations and it is determined by

$$\dot{\rho}^{prop}_{M\alpha i} = k_{\alpha i} \rho_{M\alpha i} \left| v_{\alpha i} \right| / \bar{r}_{M\alpha i} \, , \tag{45}$$

in which the material parameters $k_{\alpha i}$ and $\bar{r}_{M\alpha i}$ are the propagation coefficient and the average mobile dislocation loop radius of curvature.

The escape of pileup dislocations $\dot{\rho}^{esc}_{P\alpha i}$ has two sources: one is caused by thermal escape $\dot{\rho}^{esc\theta}_{P\alpha i}$ due to the thermal fluctuation with assistance of external forces, and the other $\sum_\beta \sum_j \dot{\rho}^{esc-inter}_{P\alpha i-M\beta j}$ is caused by $\rho_{P\alpha i}$ population interacting with the mobile dislocations of each slip system in each twin variant based on Eq. (40). Thermal escape term is given by

$$\dot{\rho}^{esc\theta}_{P\alpha i} = \frac{\rho_{P\alpha i}}{t^{esc\theta}_{P\alpha i}} P^{esc}_{P\alpha i} \, , \tag{46}$$

where $t^{esc\theta}_{P\alpha i}$ is the time constant equal to the average time of a thermal fluctuation, which is the mean phonon frequency; $P^{esc}_{P\alpha i}$ is defined in Eq. (34).

The evolution of pileup dislocations is given by the expression

$$\dot{\rho}_{P\alpha i}=\sum_{B}\sum_{\beta}\sum_{j}\dot{\rho}_{M\alpha i-B\beta j}^{pile-Mai}-\dot{\rho}_{P\alpha i}^{escT}-\sum_{\beta}\sum_{j}\dot{\rho}_{P\alpha i-M\beta j}^{esc-inter}-\dot{\rho}_{M\alpha i-P\alpha i}^{anni-MP}-\sum_{\beta}\sum_{j}\dot{\rho}_{P\alpha i-M\beta j}^{lock-inter}. \tag{47}$$

Eq. (47) shows that pileup dislocations are generated due to the pileup of mobile dislocations, and its population reduces due to the escape, annihilation, and lock formation. It is noted that the annihilation of $\rho_{P\alpha i}$ cannot caused by $\rho_{P\alpha i}$ itself because the zero velocity of pileup dislocations. This evolution is only caused by $\dot{\rho}_{M\alpha i-P\alpha i}^{anni-MP}$ and defined in Eq. (40).

Locked sessile dislocations do not belong to any slip system. However, they do affect motion of mobile dislocations and affect the escape of pileup dislocations, which is considered in Eqs. (34) and (36). They do not have interactions with itself or they do not interact with other dislocations by Eq. (40). The density of locked dislocations increases as mobile dislocations interact with mobile or pileup dislocations to leave sessile locked debris in the materials

$$\dot{N}^{L}=\sum_{M\alpha i}\sum_{B\beta j}N_{M\alpha i-B\beta j}^{lock}=\sum_{M\alpha i}\sum_{B\beta j}P_{M\alpha i-B\beta j}^{lock}D_{M\alpha i-B\beta j}^{lock}f_{M\alpha i-B\beta j}^{lock}N_{M\alpha i}N_{B\beta j}\left|\boldsymbol{v}_{A\alpha i-B\beta j}\right|. \tag{48}$$

Note that $f_{M\alpha i-B\beta j}^{lock}$ controls the fraction of collisions that form locks. The value of $P_{M\alpha i-B\beta j}^{lock}=1$ was used previously (Hansen et al, 2013) because the energy releases during the formation of locks.

The velocity gradient attributed to all dislocation slip is therefore given by

$$\dot{\mathbf{F}}_{sl}\cdot\mathbf{F}_{sl}^{-1}=\sum_{i}\sum_{\alpha}c_{i}\dot{\gamma}_{\alpha i}\left(\mathbf{s}_{\alpha i}\otimes\mathbf{m}_{\alpha i}\right),\qquad\dot{\gamma}_{\alpha i}=b_{\alpha i}\rho_{M\alpha i}v_{\alpha i}. \tag{49}$$

Since the sign of $\dot{\gamma}_{\alpha i}$ is determined by mobile dislocation velocity $v_{\alpha i}$ in Eq. (49) and the resolved shear stress $\tau_{\alpha i}=\mathbf{F}_{e}^{-1}\cdot\boldsymbol{\sigma}\cdot\mathbf{F}_{e}:\left(\mathbf{s}_{\alpha i}\otimes\mathbf{m}_{\alpha i}\right)$ in Eq. (20) determines the sign of $v_{\alpha i}$ in Eq. (31), the signs of $\dot{\gamma}_{\alpha i}$ and $\tau_{\alpha i}$ remain the same all the time. Consequently, the second law of thermodynamics in Eq. (19) is always satisfied and the plastic slip process is thermodynamically consistent in our model.

4.3 Deformation twinning flow rule.

The mechanical twinning in single crystal titanium was studied by Salem et al. 2005. The representation for twinning in this paper is developed based on their work. The driving force for

twinning was developed in Section 3, which yields $\tau_{tw-i} = \mathbf{F}_{sl}^{-1} \cdot \mathbf{F}_e^{-1} \cdot \boldsymbol{\sigma} \cdot \mathbf{F}_e \cdot \mathbf{F}_{sl} : \mathbf{b}_i \otimes \mathbf{n}_i$ applied on the $\mathbf{b}_i, \mathbf{n}_i$ twin system. The velocity gradient due to twinning is represented by

$$\dot{\mathbf{F}}_{tw} \cdot \mathbf{F}_{tw}^{-1} = \sum_{i=1}^{n} \dot{c}_i \gamma_{tw} \mathbf{b}_i \otimes \mathbf{n}_i \,, \tag{50}$$

where γ_{tw} is the constant shear strain associated with twinning and its magnitude varies with twin system. The summation of i is from 1 to the number of twins n, excluding the untwinned material 0. The power law for evolution of twins based on Salem et al. (2005) and used here is as follows

$$\dot{c}_i = \begin{cases} 0 & if\ \tau_{tw-i} < \tau_{tw0} \\ \left(1 - c_i^{b_0}\right) \dfrac{\dot{\gamma}_0}{\gamma_{tw}} \left(\dfrac{\tau_{tw-i}}{S_{tw}} \right)^{d_0} & if\ \tau_{tw-i} \geq \tau_{tw0} \end{cases}, \tag{51}$$

where positive τ_{tw0} is the material constant that the shear stress must reach to initiate the twinning process; $\dot{c}_i$ is the concentration rate for the twinned variants $(i \neq 0)$. The quantity $\dot{\gamma}_0$ is the reference shear rate; and S_{tw} with initial value S_{tw0} can be updated based on

$$\dot{S}_{tw} = h_{tw} \left(\sum_i \gamma_{tw} \dot{c}_i \right) \left(\sum_c c_i \right)^{e_0} + h_{sl} \left(\sum_j \sum_\alpha c_j \dot{\gamma}_{\alpha j} \right)^{f_0} \left(\sum_j \sum_\alpha c_j \gamma_{\alpha j} \right)^{g_0} \,, \tag{52}$$

in which $\left(\sum_i \gamma_{tw} \dot{c}_i \right)$ denotes the equivalent shear rate of the i-th twin system; the summation of i is from 1 to the number of twinned variants; $\sum_j \sum_\alpha c_j \gamma_{\alpha j}$ represents the total shear strain accommodated by plastic slip of both untwinned and twinned regions ($\gamma_{\alpha j}$ is from Eq. (49)), and j starts from 0 to the number of twinned systems. The plastic slip within twins was not considered in Salem et al. 2005. In Eq. (52), h_{tw}, h_{sl}, d, e_0, f_0 and g_0 are the material parameters. From Eq. (51), both $\dot{c}_i$ and τ_{tw-i} are positive, which assure that the second law of

thermodynamics in Eq. (23) for the twinning process is always satisfied and our deformation twinning flow rule is thermodynamically consistent.

Levitas (1998) and Levitas and Javanbakht (2015) discussed the inheritance of parameters and state variable quantities of plastic slip during phase transformations in detail. For example, in these two references the explicit expression is given for the Schmid tensor of the parent phase in the product phase when phase transformation occurs. Since twinned variants have different lattice orientations from the original parent material, the number of slip systems remain the same and the Schmid tensor will simply be rotated in this paper. This belongs to a special case of phase transformations as in Levitas (1998) and Levitas and Javanbakht (2015): the Schmid tensor of the parent phase after phase transformation is coincided with the Schmid tensor of the product phase.

One of the questions in this area is how the dislocation density varies during twinning. It is physically reasonable to assume that when the variant *I* transforms to variant *J* over a short time Δt, the newly transformed small amount of variant *J* has the same properties (including dislocation density) with the current existing variant *J*. By this means, we can update dislocation density during twinning. In the opposite, if the newly transformed region has very different properties (including dislocation density) with the current variant *J*, this will potentially cause a large internal stress between the preexisting and newly formed variant *J*, which may not be physically reasonable unless we apply a very large driving force for such processes. In addition, it is also commonly assumed that the dislocations and dislocation density are inherited from the parent to product phase during phase transformations, in which dislocation structure rotates with the lattice. Therefore, in this special case of deformation twinning, it seems more reasonable to assume that the newly transformed product has the same dislocation density with the preexisting one and therefore this is followed here.

4.4 Secondary and higher order twinning

Since the theory with the primary twinning is developed above, including any order of twinning is similar. For secondary twinning, the rotation tensor of the lattice $\mathbf{R}_{2s}$ from the parent material yields,

$$\mathbf{R}_{2s} = \mathbf{R}_2 \cdot \mathbf{R}_1 , \tag{53}$$

in which $\mathbf{R}_1$ is the lattice rotation of the primary twin region, and $\mathbf{R}_2$ is the lattice rotation of the secondary twin region relative to the primary twin material. In general then, for the *n*-th order twinning the rotation tensor $\mathbf{R}_{ns}$ relative to the un-twinned parent material can be written as

$$\mathbf{R}_{ns} = \mathbf{R}_n \cdot ... \cdot \mathbf{R}_2 \cdot \mathbf{R}_1 . \tag{54}$$

In the elasticity rule in Eq. (24), we need the summation with respect to all variants, and the elastic constants for the *n*-th order twinned variant with the rotation matrix in Eq. (54) can be written as

$$\mathbf{C}_i = C_{0-lmjk} \left(\mathbf{R}_{ns} \cdot \mathbf{e}_l\right)\left(\mathbf{R}_{ns} \cdot \mathbf{e}_m\right)\left(\mathbf{R}_{ns} \cdot \mathbf{e}_j\right)\left(\mathbf{R}_{ns} \cdot \mathbf{e}_k\right). \tag{55}$$

For plastic slip, there are of course greater numbers of active slip systems overall if the higher order of twinning is considered. In Eq. (49), we sum up the contributions from the slip systems of all levels of twinned variants and parent material. The Schmid tensor and the driving force for plastic slip in the *n*-th order twin variant are

$$\mathbf{s}_{\beta-ns} \otimes \mathbf{m}_{\beta-ns} = \mathbf{R}_{ns} \cdot \left(\mathbf{s}_{\beta 0} \otimes \mathbf{m}_{\beta 0}\right) \cdot \mathbf{R}_{ns}^T , \quad \tau_{\beta-ns} = \mathbf{F}_e^{-1} \cdot \boldsymbol{\sigma} \cdot \mathbf{F}_e : \left(\mathbf{s}_{\beta-ns} \otimes \mathbf{m}_{\beta-ns}\right) , \tag{56}$$

where β varies from 1-15 representing 12 pyramidal and 3 prismatic slip systems.

The rotation rule of the Schmid tensor for twinning is slightly different from Eq. (56). The Schmid tensor for primary twinning is $\left(\mathbf{b}_i \otimes \mathbf{n}_i\right)$ without being multiplied by $\mathbf{R}_i$, but in Eq. (56) we have the Schmid tensor for slip within the primary twin region $\mathbf{R}_i \cdot \left(\mathbf{s}_{\beta 0} \otimes \mathbf{m}_{\beta 0}\right) \cdot \mathbf{R}_i^T$. The rotation tensor for the Schmid tensor $\left(\mathbf{b}_i \otimes \mathbf{n}_i\right)$ of the *n*-th order twinning is $\mathbf{R}_n^{-1} \cdot \mathbf{R}_{ns}$ and the driving force for the *n*-th order twinning is

$$\tau_{tw-i} = \mathbf{F}_{sl}^{-1} \cdot \mathbf{F}_e^{-1} \cdot \boldsymbol{\sigma} \cdot \mathbf{F}_e \cdot \mathbf{F}_{sl} : \left[\left(\mathbf{R}_n^{-1} \cdot \mathbf{R}_{ns}\right) \cdot \left(\mathbf{b}_i \otimes \mathbf{n}_i\right) \cdot \left(\mathbf{R}_{ns}^{-1} \cdot \mathbf{R}_n\right)\right] . \tag{57}$$

It is noted that in Eq. (54), $\mathbf{R}_n, \cdot ... \cdot, \mathbf{R}_2, \mathbf{R}_1$ are the rotation tensors in the global coordinate system, and they are not directly obtained from Eq. (25), because the normal direction of twinning plane is rotated during each twinning process. Eq. (25) directly represents the rotation tensor for each twinning process $\mathbf{R}_k'$ in the local coordinate system $(x'y'z')$, in which the x' axis is along a_1 and z' is along the *c* axis of previous order (*k*-1) variant. Further, Eq. (54) can be rewritten as

$$\mathbf{R}_{ns} = \mathbf{R}_n \cdot ... \cdot \mathbf{R}_2 \cdot \mathbf{R}_1 = \mathbf{R}'_1 \cdot \mathbf{R}'_2 \cdot ... \cdot \mathbf{R}'_n \,, \tag{58}$$

Such a relation in Eq. (58) is obtained in the same way for rotation tensors from Euler angles by rotations based on global (extrinsic rotation) and local coordinate systems (intrinsic rotation). Obviously, by using local coordinate systems, obtaining the rotation tensor is more straightforward. For higher order twinning, inheritance of history state variables follows the same assumption as taken for primary twin regions.

4.4 Material parameters for slip and twinning.

Metals having an HCP crystal structure, generally display prismatic $\langle a \rangle$, pyramidal $\langle a+c \rangle$, and basal slip modes. In the case of titanium, pyramidal $\langle a+c \rangle$ and prismatic $\langle a \rangle$ slips are the active modes (Clouet et al., 2015; Nervo et al., 2016; Yoo et al., 2001; Morrow et al, 2016), which are shown in Fig. 1 (a) and (b). Based on the symmetry, there are 12 pyramidal slip systems (k=1, 2, 3, …, 12) and 3 prismatic slip systems (k=13, 14, 15). In this paper, a Cartesian coordinate system is used and drawn in Fig. 1 (a) for the single crystal loaded in the [0001] direction (i.e. c axis), where the z axis is along the c axis of the single crystal of the parent material, and the x axis is along the a_1 axis. In Section 5, the slip systems k=1, and k=13, 14, 15 will be discussed. The slip normal and slip direction for pyramidal slip k=1 in the parent material is (0, 0.8776, 0.4793) and (0.2667, -0.4620, 0.8458). For prismatic slip k=13, 14, 15 at the parent material, the slip normal is (0, 1, 0), (0.866, -0.5, 0.0), and (0.866, 0.5, 0.0), respectively. The other slip directions can be easily obtained by using lattice length ratio c/a = 0.4699 nm/0.2937 nm = 1.5856. Six tensile $\{10\bar{1}2\}\langle\bar{1}011\rangle$ and six compressive $\{11\bar{2}2\}\langle 11\bar{2}\bar{3}\rangle$ twinning modes in Fig. 1 (c) and (d) are commonly observed to be active for simple compression deformation in zirconium and titanium single crystals (Beyerlein and Tomé, 2008; Morrow et al., 2016). Because twinning only occurs in either the positive or negative direction of $\mathbf{b}_i$, we need to define both $\mathbf{b}_i$ and $\mathbf{n}_i$ at the same time. In Fig. 1 (c) and (d) the purple arrows stand for the outward normal of the twinning plane and corresponding twinning directions are marked in red. If the red arrows switch into the opposite directions, purple arrows must change directions as

well to keep $\mathbf{b}_i \otimes \mathbf{n}_i$ unchanged. This is different from the representation of slip systems because slip can occur in both the positive and negative directions of the red arrows in Fig. 1 (a) and (b).

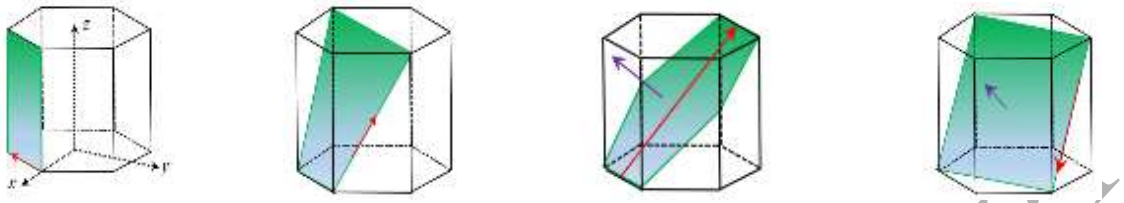

(a) (b) (c) (d)

Fig. 1. Slip and twinning systems. Prismatic slip mode (a), pyramidal slip mode (b), tensile twinning (c), and compressive twinning (d). The red arrow stands for the slip or twinning direction. The purple arrow stands for the outward normal direction of the twinning plane.

The Burgers vectors magnitude in the pyramidal and prismatic slip modes are 0.55 nm and 0.29 nm, respectively (Yoo et al., 2001). It is known that the dislocation with a larger Burger vector has a greater resistance to motion (Gong et al., 2015), and thus salient differences in the inherent lattice resistance $\tau_0^{\alpha,i}$ in Eq. (35) are found for the prismatic $\left(\tau_0^{\alpha,i} = 37\,\mathrm{MPa}\right)$ and pyramidal $\left(\tau_0^{\alpha,i} = 800\,\mathrm{MPa}\right)$ slip modes (Beyerlein and Tomé, 2008). The simulations in Section 5 will show that pileup dislocations can easily escape and become mobile again for the prismatic slip mode with the assistance of the external stress, which is not the case for the pyramidal slip mode due to a large $\tau_0^{\alpha,i}$. Like in Hansen et al. (2013), the unknown fractional coefficients for dislocation locking $f^{L}_{A\alpha i-B\beta j}$ and escaping f^{esc} during dislocation interactions are left for future investigation and set to zero in this paper; in addition, we accept that initial dislocation density at *t*=0 are only within the mobile population and are equal in all slip systems ($\rho_{M\alpha i} = 4.1\times10^{9}\,\mathrm{m}^{-2}$). During the interaction of dislocations on two slip systems, as we discussed before for mobile dislocation density $N_{M\alpha i}$, pile-up and annihilate on itself $f^{pile-itself}_{M\alpha i-B\beta j} = f^{anni-itself}_{M\alpha i-B\beta j} = 1/4$. In addition, we use $f^{pile-MP}_{M\alpha i-P\alpha i} = f^{anni-MP}_{M\alpha i-P\alpha i} = 1/8$ in this paper because our simulations show that the total pileup dislocation density is smaller than mobile dislocation density. In Eq. (34), $k_b = 1.38\times10^{-23}\,\mathrm{J\cdot K}^{-1}$ is used (Alankar et al., 2011) and room temperature as Θ = 298 K. Other material parameters used for plastic slip are shown in Table 2. For simplicity, hardening for twinning in Eq. (52) is

ignored, and the parameters in Eq. (51) are listed in Table 3. As we found in experiments in Morrow et al. (2016), single crystal titanium loaded in both $[0001]$ and $[10\bar{1}1]$ directions undergoes compressive twinning as primary twinning and tensile twinning as secondary twining, which are considered in our simulations. In table 3, the shear strain γ_{tw} has two different values because there are different expressions for compressive and tensile twinning and they can be found from Yoo (1991). In Eq. (51), unlike in Salem et al. (2005), τ_{tw0} is not zero in this paper. While there is no thermal barrier between the parent and twinned variants, the athermal dissipation during twinning mostly related to interface friction cause a nonzero τ_{tw0}. It is found that for the HCP titanium under the dynamic loading conditions examined in this manuscript, primary twinning readily occurs so we use a small value of 20 MPa for τ_{tw0} in Table 3. As shown in Fig. 6 (b), twinning occurs at the very beginning of loading. The secondary twinning occurs later in the deformation history and therefore the resistance to formation is expected to be greater, consequently τ_{tw0} and S_{tw0} have larger values in the secondary twinning. In addition, we only consider the plastic slip in the parent material and primary twins, and ignore plastic slip in the secondary twins.

Quantity (Unit)	L (nm)	$k_1 \cdot \mu$ (GPa)	$k_{\alpha i}/\bar{r}_{M\alpha i}$ (1/m)	B_0 (Pa*s)	$D_{M\alpha i-P\alpha i}^{pile-MP} = 2D_{M\alpha i-B\beta j}^{pile-itself}$ (m^{-2})	$D_{M\alpha i-P\alpha i}^{anni-MP} = 2D_{M\alpha i-B\beta j}^{anni-itself}$ (m^{-2})	m (kg/m)
Magnitude	40.0	3*46.7	1e-4/2.1e-6	2.2e-4	4.8e-9	2.4e-9	3e-17

Table 2. Single crystal titanium material parameters for plastic slip.

Quantity (Unit)	b_0 (1)	γ_{tw} (1)	S_{tw0} (MPa)	$\dot{\gamma}_0$ (1/s)	τ_{tw0} (MPa)	d_0 (1)
Magnitude	0.53	0.216 (primary) /0.177 (secondary)	970 (primary) /2425(secondary)	1.0e4	20 (primary) /120(secondary)	1.48

Table 3. Single crystal titanium material parameters for twinning. When there is no note in primary or secondary twinning, it means the value for both.

5. Simulations on single crystal titanium deformed by SHPB

5.1 Geometry and boundary conditions for the [0001] specimen

High-purity (99.99%) single crystal titanium was impacted under SHPB at Los Alamos National Laboratory (Morrow et al, 2016). From the experiments, the single crystal titanium specimens were right circular cylinders (1.255 mm in radius and 2.46 mm in length) and the loading is along both the $\left[10\bar{1}1\right]$ direction and the *c* axis of the crystal lattice [0001] of single crystal, which are used in simulations. We will call these two specimens under such two loading directions as the [0001] specimen and the $\left[10\bar{1}1\right]$ specimen. In Section 5.1 and 5.2, we discuss the case of the [0001] specimen, and the $\left[10\bar{1}1\right]$ specimen will be analyzed in Section 5.3. The global coordinate system for the [0001] specimen is that the x axis is along the a_1 and z is along the *c* axis of the parent material as shown in Fig. 1 (a). The schematic of the numerical model used to represent the experiments is presented in Fig. 2: on the left end the displacement u_z in the z axis direction is fixed as zero, and on the right end, we applied the displacement u_z. The curved surface of the cylinder is stress free with unimpeded displacement. In the experiments, the displacement along the z axis can be directly measured during the loading process and is shown in Fig. 2 (b). In simulations of the experiment this displacement versus time loading profile u_z is applied to the model shown in Fig. 2 (a). We then compare the load versus time profile between the experiment and simulation results. More detail of the experiments and numerical analysis of the structural evolution can be found in Morrow et al. (2016).

The constitutive equations in Section 4 are implemented into a user defined material subroutine (VUMAT) in the FEM code ABAQUS EXPLICIT. Our results are not time-step size and mesh size dependent. Specifically, we divided the total loading time into 1,578 and 3,115 equal-time steps, and assigned 3,164 and 7,254 elements in the titanium sample with the element type as an 8-noded brick element (C3D8). For all of these cases, we obtained the same simulation results.

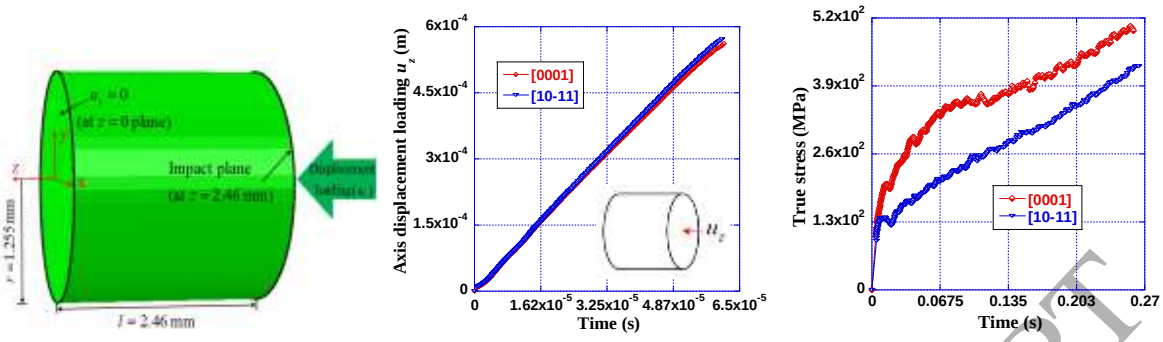

(a) (b) (c)

Fig. 2. The geometry and boundary conditions of the titanium sample for both [0001] specimen and $\left[10\bar{1}1\right]$ specimen (a), the variation of the axial displacement u_z at the impact plane with respect to the rising loading time *t* for both simulation and experiment for the [0001] and $\left[10\bar{1}1\right]$ specimens (b), and the true stress versus strain curve from experiment for both specimens (c).

5.2 Discussion of results for the [0001] specimen

The titanium sample under SHPB loading is generally subjected to deformation of moderate magnitude. The true stress versus true strain for the [0001] specimen in experiment can be found in Fig. 2 (c), where the maximum strain reaches around 0.25. In comparison with Fig. 3 (a), Fig. 3 (b) shows that the compressive deformation along the *z* axis and tensile deformation in the radial direction are both finite. Since in our simulation we apply the same u_z vs. time profile with experiment, and thus the true strain versus time also remains the same between simulation and experiment as illustrated in Fig. 2 (b). As discussed in Section 4.1, the elasticity of single crystal titanium is not highly anisotropic. In addition to the parent material, Fig. 4 (d) shows that there are six compressive twin variants (i.e. primary twins) and they are along six symmetry directions with respect to the *z* axis, which makes twinning close to a globally isotropic process in spite of a slight anisotropy caused by the secondary twinning. The coexistence of 15 variants in Fig. 4 (d) with different crystallographic orientations makes the average aggregate elasticity even closer to isotropic than the undeformed single crystal. For each twin variant, there are up to fifteen slip systems available, which with increased volume fraction of twins of different variants, effectively causes the material to become more plastically isotropic as deformation progresses. Fig. 3 shows that in the entire sample, the variation of normal compressive stress is

around 0.4%, and the variation of total mobile dislocation density N^m_{total} is less than 0.4%. The initial parent material does not transform to six tensile twins as the primary twins can be easily explained by Fig. 1 (c): under uniaxial compression σ_{zz} along the *c* axis, the shear stress on the twinning plane is along the opposite direction of the red arrow (the red arrow). If uniaxial tension is applied, the shear stress will be the same with the tensile twinning direction, which can promote the tensile twinning. However, for the secondary twinning, there are several tensile twins with a small volume fraction in each one obtained as shown in Fig. 4 (d).

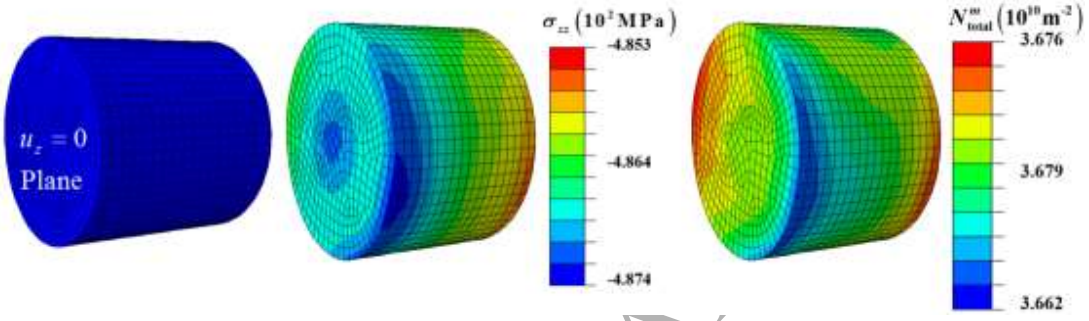

(a) (b) (c)

Fig. 3. The distributions of the normal stress σ_{zz} (b) and the total mobile dislocation density N^m_{total} (c) in the deformed configuration at the t=54.5 μs for the [0001] specimen. The undeformed configuration of the sample is presented in (a).

Fig. 5 (d) compares the results from the simulation and experiment on the true stress: F_z/A, where F_z is the total compressive force on the sample, and A is the cross-sectional area of the sample at the current time *t*. Initially close to *t*=0, the slope of the stress curve is very large, which corresponds to elastic deformation. When the plastic deformation takes place, the slope of the stress curve is reduced and in the region around t=24 μs, a plateau appears in the stress curves of both experiments and simulations, while the axial displacement (i.e. the normal strain) continues to increase during the entire loading process (see Fig. 2 (b) and (c)). In the simulation results, we find that the total dislocation density varies during the entire loading and the dislocation density in individual slip systems in each twin variant changes as well. In both experiment and simulation, we find fluctuations in the stress curve. Complex coupling among elasticity, twinning and slip and the nonlinearities within each process causes the fluctuations in

the simulation results. The stress difference in Fig. 5 (d) may be caused by the following: 1) although the model for plastic slip are advanced, there are very limited parameters used for plastic slip for 225 slip systems; (15 potential slip systems in each variant, and 14 twinned variants plus parent materials: $15\times15=225$) and 14 twinning processes (6 compressive twins and 8 tensile twins); 2) we ignore the dislocation locking and the escape of pileup dislocations during interactions of two slip systems as in Hansen et al. (2013); 3) representation of deformation twinning (prominent for this loading orientation) by a pseudo-slip model is not yet adequate; finally 4) the inheritance of dislocation structure onto the twinned regions of materials is still very much a research topic, and therefore the insights gained here are a step in that direction.

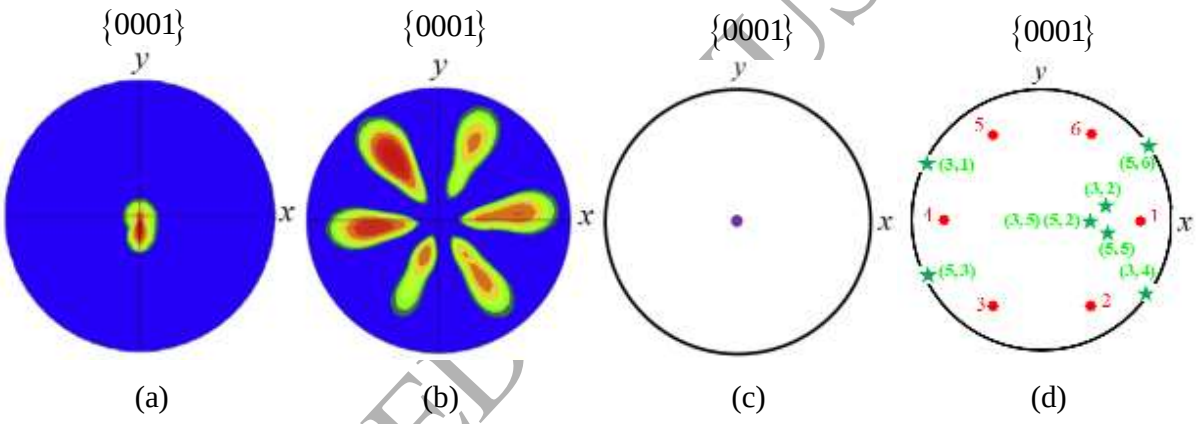

Fig. 4. The {0001} pole figures from the experimental EBSD data ((a) and (b)) in Morrow et al (2017) and current simulations ((c) and (d)), where (a) and (c) are the results before the loading, and (b) and (d) are after loading for the [0001] specimen. In (d), the primary twins are marked in red with numbers1-6; the secondary twining (tensile twinning) is marked in green with two numbers in parentheses (the first number (3 and 5) indicates which primary twin variant they are from and the second number (1-6) indicates six different tensile twinning variants)

Fig. 4 presents the {0001} pole figures from both simulations (Figs. 4 (c) and (d)) and experiments (Figs. 4 (a) and (b)) from Morrow et al (2017). From Fig. 4 (a) and (c), there is one crystal orientation which is localized at the center of the pole figures. After loading the twinned variants appear, and as shown in Fig. 4 (b) and (d) six compressive twins (primary twins) can be clearly seen with symmetry coordinates in the pole figures. From experiments (Morrow et al., 2016), the concentration of parent material for the [0001] specimen is 1%, and 99% material is twinned after loading. This is consistent with our simulation that at the final

loading the parent material is around 0.2% as shown in Fig. 6 (a). We also find a small amount of tensile twinning in Fig. 6 (c) and Fig. 4 (d). For the [0001] specimen, the experimental pole figure does not show the secondary twins due to a small volume fraction in every secondary twin, which is much smaller than the individual secondary twin volume fraction in the $[10\bar{1}1]$ specimen. In the $[10\bar{1}1]$ specimen, both the experiment and simulation pole figures clearly show the secondary twins.

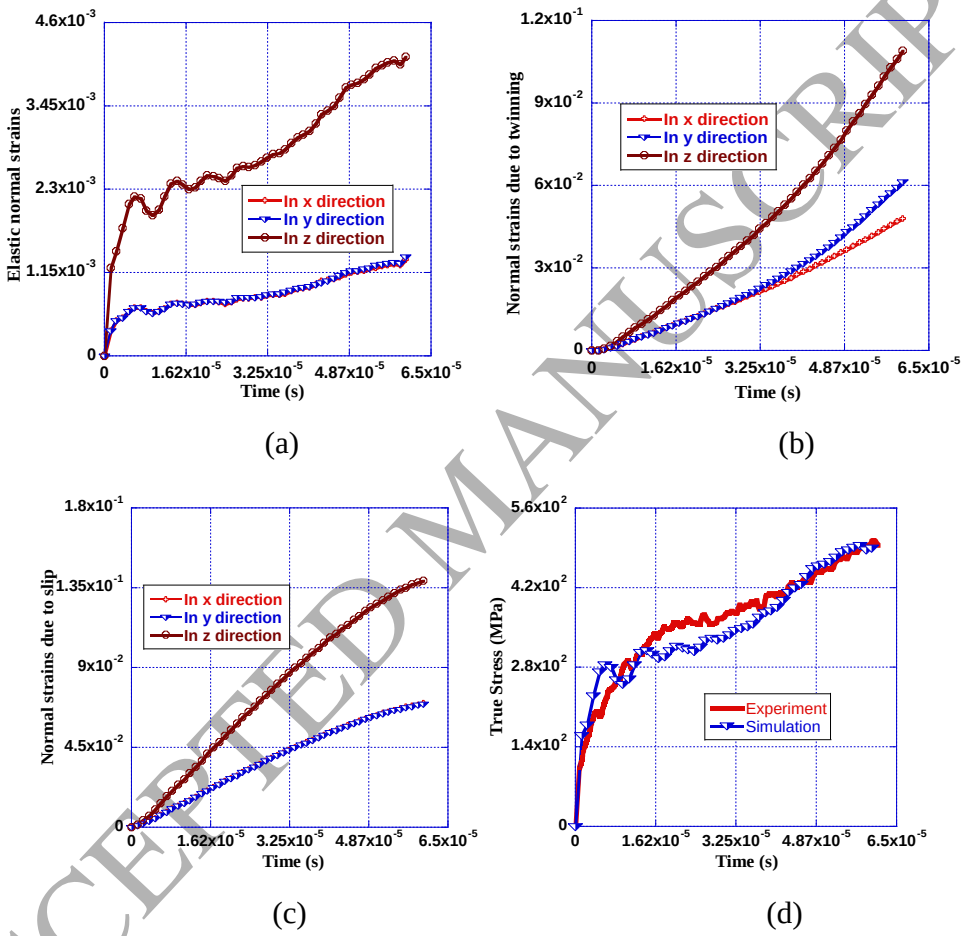

Fig. 5. Normal strains in the *x*, *y* and *z* directions for the [0001] specimen, due to elasticity: ε_{ex}, ε_{ey}, and ε_{ez} (a), due to plastic twinning ε_{twx}, ε_{twy}, and ε_{twz} (b), and due to plastic slip ε_{slx}, ε_{sly}, and ε_{slz} (c). The variation of true stress with the rising loading time *t*, in both simulations and experiments for the [0001] specimen (d).

Fig. 3 shows that there is moderately large deformation in both radial and axial directions and Fig. 5 plots the deformation contribution from each of the components: elasticity, twinning, and slip. While we only have one stress with an appreciable value, there are three normal strains with

nonzero values in the strain tensors. For normal strains in Fig. 5, their definitions are the absolute values of logarithmic strain for three diagonal components of deformation gradients ($\boldsymbol{F}_e, \boldsymbol{F}_{tw}$ and $\boldsymbol{F}_{sl}$). For example, the axial elastic normal strain is $\varepsilon_{ez} = \left|\ln F_{e33}\right|$ and in the other two directions $\varepsilon_{ex} = \left|\ln F_{e11}\right|$, $\varepsilon_{ey} = \left|\ln F_{e22}\right|$. The reason for using the logarithmic strains is that the true strain $\left|\ln F_{33}\right|$ under uniaxial loading shown in Fig. 2 (c) is also logarithm strain and have the following relation:

$$\left|\ln F_{33}\right| = \left|\ln F_{e33}\right| + \left|\ln F_{sl33}\right| + \left|\ln F_{tw33}\right| = \varepsilon_{ez} + \varepsilon_{slz} + \varepsilon_{twz}. \tag{59}$$

From Fig. 5, it is noted that during the entire loading process, the normal strains for elasticity and plasticity in the *x* and *y* directions are the same for each process: $\varepsilon_{ex} = \varepsilon_{ey}$, and $\varepsilon_{slx} = \varepsilon_{sly}$, while there is a small difference in the twinning process for ε_{twx} and ε_{twy} due to the absence of symmetry in secondary twinning. Fig. 5 shows that the major deformation is from the plastic deformation with slightly larger slip than twinning deformation, which is two orders of magnitude larger than the magnitude of elastic deformation.

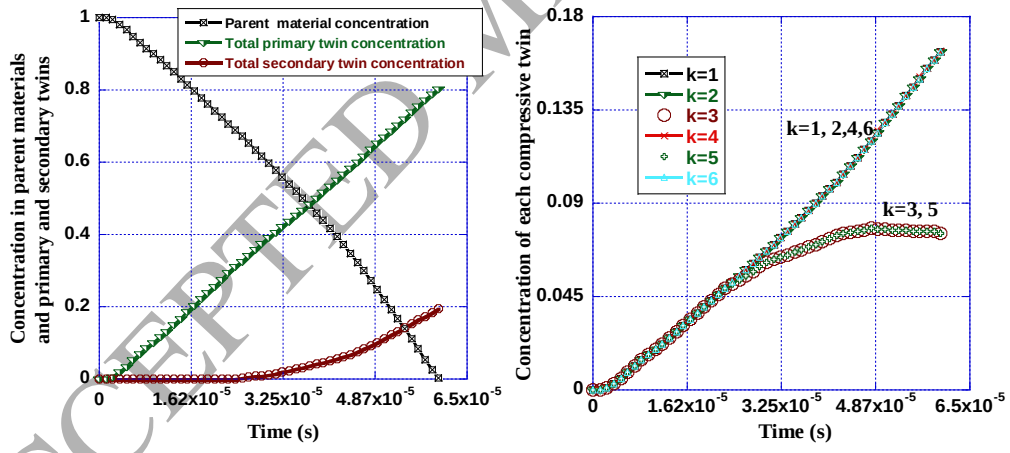

(a) (b)

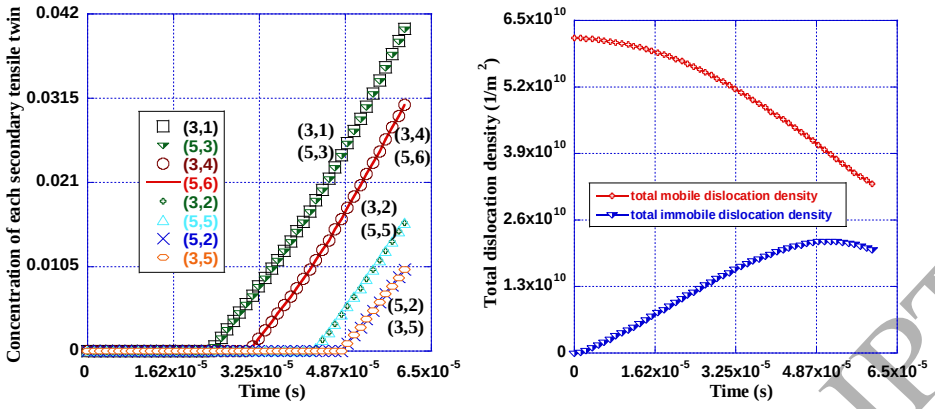

(c) (d)

Fig. 6. Variations of volume fraction of the parent material and total twinned variants (a), the volume fraction in each primary twin (b) and each secondary twin (c), and total mobile N^m_{total} and pileup N^p_{total} dislocation density of parent material and primary twins (d), for the [0001] specimen with respect to the loading time.

Fig. 6 (a) shows that during the loading process, the total twin volume fraction continues to increase, and at the end of the loading process most of material is twinned, which is consistent with experimental findings (Morrow et al., 2016). While a small amount of parent material exists in the end, the deformation caused by twinning does not account for most of the deformation displayed in Fig. 6, where plastic slip is the most dominant deformation mechanism in the sample. In Fig. 1 (d), the axial stress is along the *c* axis of the crystal lattice and has the same angle with all twin planes and twin directions, which leads to the same resolved shear stress for each compressive twin variant. Based on Eq. (51), this results in exactly the same concentration in each primary (compressive) twin variant before the secondary (tensile) twins appear, as plotted in Fig. 6 (b). The appearance of the secondary twins from primary twins number 3 and 5 causes a little anisotropy in the deformation in 7 (b), since there is no symmetry in pole figure with respect to the *z* axis as shown in 6 (d). There are eight tensile twins as shown in Fig. 6 (c), but the volume fraction of each tensile twin is quite small. The total mobile N^m_{total} and pileup N^p_{total} dislocation densities are presented in Fig. 6 (c). The total mobile dislocation density continuously decreases during the entire loading process, while the total pileup dislocation density in the material initially increases and then slightly decreases. These results are explained by Figs. 7 and 8.

Let us compare slip modes in the parent material (i=0) and the 6th compressive twin variant (i=6) in Figs. 7 and 8. Because twinning rotates the crystal lattice and slip systems, there are no similar trends for slip modes between the parent regions and the twinned variants. Figs. 7 and 8 show very different variations of mobile and pileup dislocation density and mobile dislocation velocity between these two variants. It is noted that while the twinning plane in all compressive twins has a finite angle with the z axial direction, the corresponding slip systems inside twins do not have the same rotational angle with the z axis. For example, for the slip system k=1, the 1st and 2nd compressive twins have different resolved shear stresses, which cause different mobile dislocation velocities and different dislocation density between them. In Fig. 7, we find that for the slip system k=1 (pyramidal slip mode) in the parent material, initially the mobile dislocation density ρ_M rises due to fast propagation speed, because the pyramidal plane is inclined from the z axis (i.e. the direction of σ_{zz}) and it leads to an appreciable shear stress and mobile dislocation velocity by using Eq. (31) (see Fig. 7 (c)). The rate of mobile dislocation propagation is linearly dependent of the mobile dislocation velocity in Eq. (45) and during rapid mobile dislocation propagation, the mobile dislocation density increases. At the later stage of loading, the mobile dislocation velocity in the pyramidal slip mode (k=1) of the parent material is even larger and intensifies mobile dislocation propagation, but the mobile dislocation density ρ_M is reduced because the dislocation pileup and annihilation by interaction with the slip systems in twins. At the later stage of loading, the twin concentrations are larger than at the initial stage and mobile dislocation pile up in the pyramidal plane of the parent material becomes faster, which is shown in Fig. 7 (b) (i.e. the slope for k=1 increases). For prismatic slip model (k=13) of the parent material, the mobile dislocation density continuously decreases because there is no mobile dislocation propagation because of a zero mobile dislocation velocity and a zero resolved shear stress (See that the slip plane is parallel to the z axis or σ_{zz} in Fig. 1 (a)). At the initial loading state, the concentration of the parent material is dominant and the parent material determines the trend of total dislocation density in all variants in Fig. 6 (d). While there is a slight mobile dislocation density increase in the pyramidal slip modes, it drops very fast in the prismatic slip modes (k=13, 14 and 15). Consequently, the decrease of mobile dislocation density in the prismatic plane of the parent material at the initial

loading process determines a drop of the total mobile dislocation density in Fig. 6 (d), while the mobile dislocation density increases in the pyramidal slip modes.

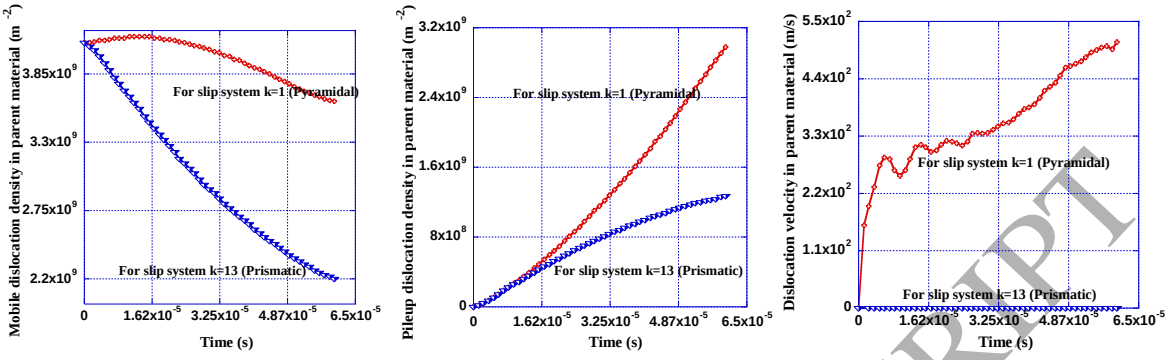

(a) (b) (c)

Fig. 7. Variations of mobile ρ_M (a) and pileup ρ_p (b) dislocation density and mobile dislocation velocity (c), for the pyramidal *k*=1 and prismatic *k*=13 slip modes of the parent material for the [0001] specimen.

Due to the lattice rotation as well as the rotation of the slip systems, the dislocation density in twin variants is very different from the dislocation density in the parent material. Specifically, in Fig. 8, mobile dislocation density ρ_M in the prismatic slip mode (*k*=13) increases but in the pyramidal slip mode (*k*=1) it decreases, for two reasons. Firstly, the propagation of mobile dislocations is faster in *k*=13 than in k=1 due to a larger velocity shown in Fig 10 (c). Secondly, the mobile dislocations pile up in *k*=1 much faster, because when the dislocations pile up in *k*=13, pileup dislocations immediately escape and become mobile again. The thermal escape of the pileup dislocations in Eq. (46) is determined by the thermal escape probability $P_{P\alpha i}^{esc}$. The magnitude of the Burgers vectors in the prismatic (*k*=13) and pyramidal (*k*=1) slip modes are 0.29 nm and 0.55 nm, respectively. The resistance to motion for dislocation with a larger Burger vector is greater, and thus salient differences in the inherent lattice resistance $\tau_0^{\alpha,i}$ in Eq. (35) are found for prismatic ($\tau_0^{\alpha,i}=37\,\mathrm{MPa}$) and pyramidal ($\tau_0^{\alpha,i}=800\,\mathrm{MPa}$) slip. A difference in the magnitude of the lattice resistance between the prismatic and pyramidal slip modes are found in HCP zirconium as well (Beyerlein and Tomé, 2008). The escape probability $P_{P\alpha i}^{esc}=1$ in *k*=13 of the 6th compressive twin since the resistance for the escape of pileup dislocation is easy to overcome with the existence of the external stress by using Eq. (34). However, in *k*=13 of the

parent material in Fig. 7 (a), the $P_{P\alpha i}^{esc}$ is much smaller than 1 because there is no shear stress on that slip plane due to its lattice orientation and the thermal escape of pileup dislocations only depends on thermal fluctuations.

Fig. 8 (d) shows that even in the same twin variant for the same type of slip mode (e.g. the prismatic slip mode), the evolution of the dislocation density among *k*=13, 14 and 15 can be very different. For *k*=13 and *k*=14, the pileup dislocations ρ_p escape immediately after mobile dislocations pile up, which is not the case for *k*=15. After twinning, the slip plane *k*=15 is still parallel to the compressive loading direction (i.e. the *z* axis), and the shear stress on the slip plane is zero. However, for the other two prismatic modes, the shear stresses are large since there is a nonzero angle between the slip planes and the compressive direction. There are 12 pyramidal slip systems and only 3 prismatic slip systems so that the pyramidal slip systems determine the trend of total mobile dislocation in twinned variants in Fig. 8 (a). At the late stage of loading, most of the material has twinned and the total mobile dislocation density is reduced (Fig. 6 (d)) and is due to the reduction of mobile dislocation density in the pyramidal planes of the twinned variants as shown in Fig. 8 (a) for pyramidal slip mode (*k*=1). Initially the pileup dislocation density is assumed as zero. During the loading process, the pileup dislocation density in both primary twins and parent regions increases, which is the reason why the total pileup dislocation propagates during most of loading process in the Fig. 6 (d). At the later stage of loading, the total pileup dislocation density in Fig. 6 (d) reduces, which is caused by secondary twinning and the total pileup dislocation density is a summation only in the parent and the primary twins.

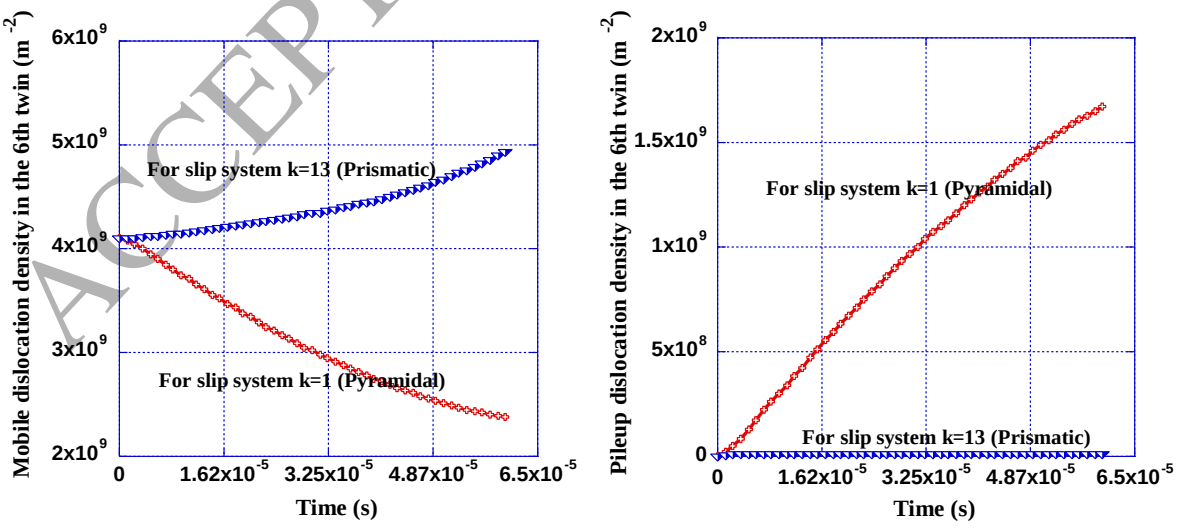

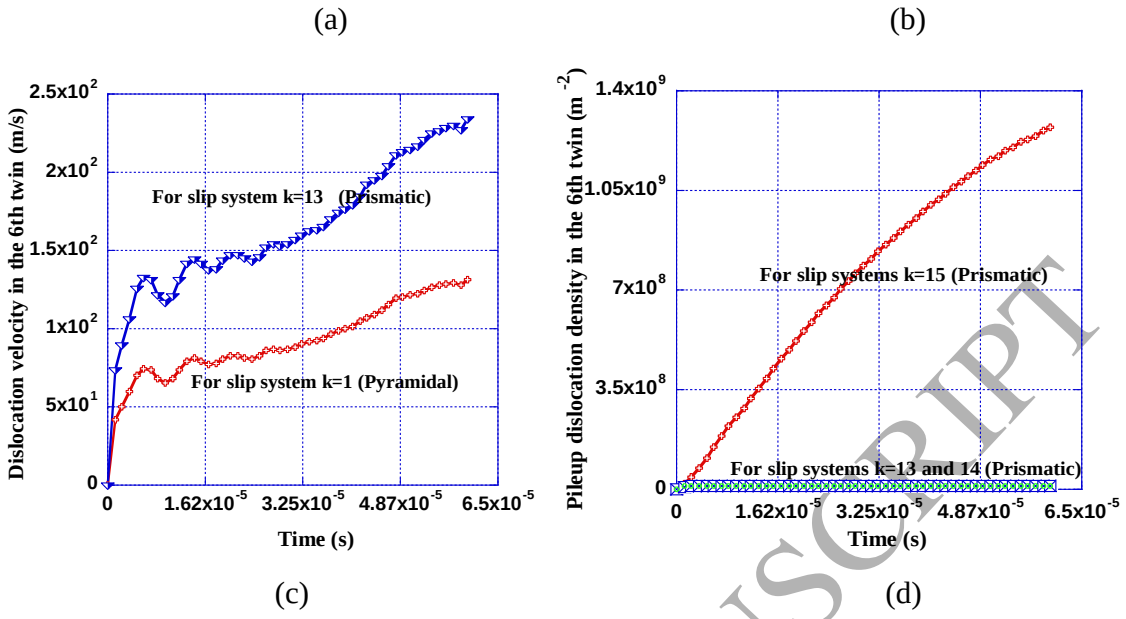

Fig. 8. Variations of mobile ρ_M (a) and pileup ρ_p (b) dislocation density and mobile dislocation velocity (c), for the pyramidal k=1 and prismatic k=13 slip modes of the 6th compressive twin when the twinning direction is along (0.2667, -0.4620, -0.8458). The variations of the pileup dislocation density ρ_p at the prismatic slip systems k=13, 14 and 15 of the 6th compressive twin (d).

5.3 Discussion of results for the $[10\bar{1}1]$ specimen

Single crystal titanium loaded in the $[10\bar{1}1]$ direction is discussed in this section. The size of the initial undeformed specimen is the same as the [0001] specimen, shown in Fig. 2 (a). Distinct from the case with the [0001] specimen, the z axis in the global coordinate system is not along the c axis of parent material but along the loading direction. It is accepted that the local coordinate system in the parent material is $x'y'z'$ with the x' axis along the a_1 and z' along the c axis of the parent material. First, we rotate the $x'y'z'$ coordinate system with +30 degrees (the positive sign + is according to the right-hand rule) with respect to the z' axis and obtain a new coordinate system $x''y''z''$ where the y'' axis is perpendicular to the plane with the z' and z axes in it. Second, we rotate the $x''y''z''$ coordinate system with +47.53^o with respect to the y'' axis (i.e. the z' or z'' axis goes to the z axis) and obtain our global coordinate system xyz. During such rotations, the rotation tensor from the $x'y'z'$ to xyz coordinate system is

$$\mathbf{R}_0 = \begin{bmatrix} 0.6752, & 0.3688, & 0.6388 \\ 0, & 0.8660, & -0.5 \\ -0.7376, & 0.3376, & 0.5847 \end{bmatrix}. \quad (60)$$

The Schmid tensors and material stiffness of parent material and twin variants defined previously in the [0001] specimen need to be rotated into the global coordinate system by this rotation tensor $\mathbf{R}_0$. The displacement loading at the impact plane of the $[10\bar{1}1]$ specimen along the *z* axis is measured experimentally during the loading process and is shown in Fig. 2 (b), and this loading profile is used in our simulation. In Fig. 2(b), the displacement loading (i.e. total deformation) applied in the $[10\bar{1}1]$ and [0001] samples are very similar. In experiments (Morrow et al., 2016), much lower concentration of twins were observed in the $[10\bar{1}1]$ specimen as compared to the [0001] specimen. This means that plastic slip deformation (i.e. less twinning deformation) plays a greater role in the $[10\bar{1}1]$ specimen since the total deformation is similar. Consequently, there is a larger mobile dislocation density in the $[10\bar{1}1]$ specimen and we assume that initial dislocation density $\rho_{M\alpha i} = 32\times10^{9}\,\mathrm{m}^{-2}$ and mobile dislocation propagation rate is $k_{\alpha i}/\bar{r}_{M\alpha i} = 357\ \mathrm{m}^{-1}$. To obtain a consistent twin volume fraction in our simulation with experiments, we use the twinning rate $\dot{\gamma}_0 = 6.7\times10^{4}\mathrm{s}^{-1}$. For all other parameters, we keep them consistent with those for the [0001] specimen.

For the [0001] specimen, the distributions of stress and dislocation density are very homogenous throughout the specimen, and due to the multiple slip modes and twin orientations for the $[10\bar{1}1]$ specimen, they only vary slightly in the sample. We will present the results at the center of the impact plane for strain curves, the pole figure, and the concentrations of variants, where is close to the average values for the impact plane.

During the entire loading process, the stress-strain curve for the $[10\bar{1}1]$ specimen is lower than the one for the [0001] specimen. For both cases, the stress variations in our simulation gives good correspondence with experiment as shown in Fig. 9 (a) and Fig. 5 (d). Fig. 10 shows that before loading, there is only one pole with a large angle between the $\boldsymbol{C}$ axis of the single crystal and the *z* axis, and after loading, there are several twin variants formed. From the

simulation, we can explain that in the experimental pole figure, the type of the twin variants belong to the primary or secondary twins and we can identify which primary twin region the secondary twins originate. We can find corresponding variants for all locations in the experimental pole figure in Fig. 10. There are four primary (compressive) twins marked in red in Fig. 10 (d), and there are four secondary (tensile) twins marked in green. The secondary twins are from the number 3 and 5 primary twin variants. The twinning directions for both primary and secondary twins are not symmetrical with respect to the *z* axis (i.e. the loading direction), which causes moderate heterogeneity in stress and dislocation density distributions in the specimen.

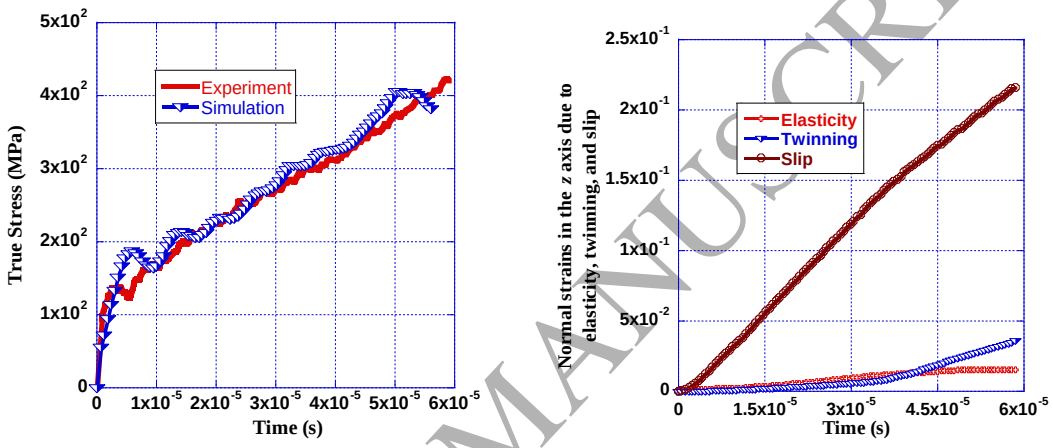

(a) (b)

Fig. 9. The variation of true stress with the rising loading time *t*, in both simulation and experiment (a). Normal strains along the *z* axis, due to elasticity ε_{ez}, plastic twinning ε_{twz}, and plastic slip ε_{slz} (b) for the $[10\bar{1}1]$ specimen.

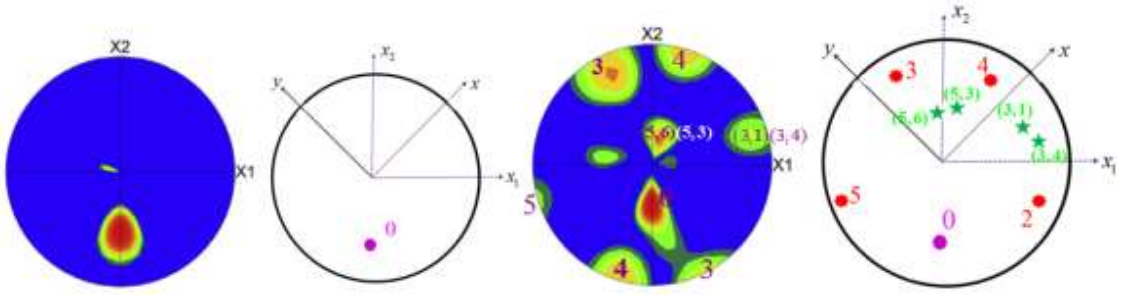

(a) (b) (c) (d)

Fig. 10. The pole figures for the $[10\bar{1}1]$ specimen from the experimental EBSD data ((a) and (c)) in Morrow et al (2017) and current simulations ((b) and (d)) with the *z* axis pointing out of the plane, where (a) and (b) are the results before the loading, and (c) and

(d) are after loading. In (d), the primary twins are marked in red with number 2, 3, 4 and 5, and the secondary twins are marked in green with two numbers in parentheses.

Fig. 2 (c) shows that a large strain of about 0.25 is applied to the specimen, and Fig. 9 (b) shows the relative strain contributions among plastic slip, elasticity, and twinning components. Plastic slip is the largest contribution in Fig. 9 (b), which is much larger than the other two deformations, and the twinning deformation is slightly larger than the elastic deformation at the end of loading. At the later stage of loading, the slope in the twinning deformation curve in Fig. 9 (b) increases, which is caused by the secondary twinning shown in the Fig. 11. In the [0001] specimen almost all of the parent material is twinned, but for the $[10\bar{1}1]$ specimen 39% of the parent material remains at the end of loading as shown in Fig. 11 (a). This is consistent with the experimental volume fraction of parent material of 44% (Morrow et al., 2016). Fig. 11 (b) shows that the number 2 and 4 primary twin variants monotonously grow, but the number 3 and 5 variants increase until they start to transform into the secondary twins. We set up a minimum as 0.05 for the primary twins, below which they do not transform into the secondary twins and corresponds to the flat part of the primary twin numbers 3 and 5 at the late loading stage. Fig. 11 (d) plots the total mobile and pileup dislocation density in the parent and primary twins. Mobile dislocation density continues to decrease and at the end of the loading process it is smaller than pileup dislocation density. Pileup dislocation density initially increases from zero and after some loading time, it starts to reduce slightly. This slight reduction is caused by the secondary twinning and the total pileup dislocation density is a summation only in the parent material and the primary twins.

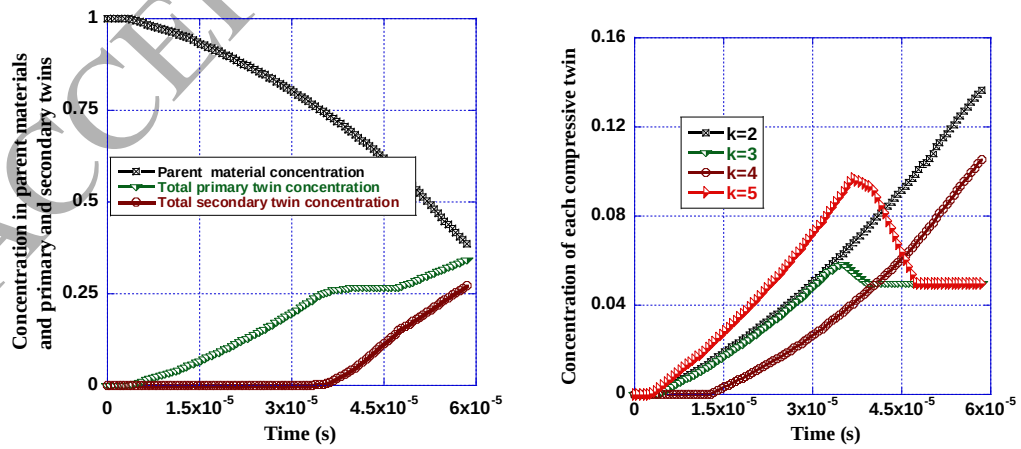

(a) (b)

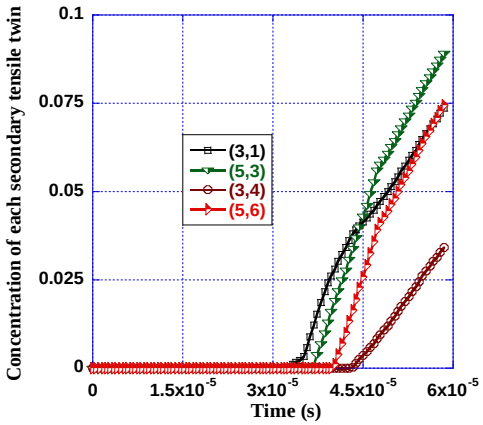

(c)

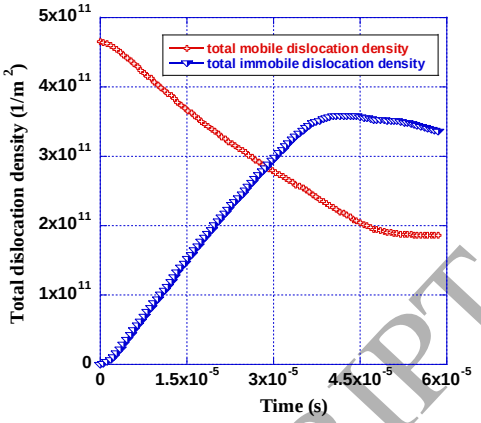

(d)

Fig. 11. Variations of volume fraction of the parent material and total primary and secondary twinned variants (a), the volume fraction in each primary twin variants (b) and secondary twin variant (c), and total mobile N^{m}_{total} and pileup N^{p}_{total} dislocation density (d), with respect to time. The location for all curves is located at the center of the impact plane.

6. Concluding remarks

In this paper, coupled elasticity, twinning, and slip in high-purity single crystal titanium deformed by SHPB are investigated, in the framework of large deformation single crystal theory. A thermodynamically consistent system of equations is formulated for large elastic, slip, and twinning deformation mechanisms. Novel kinematics is proposed to consider plastic slip in all parent and twin variants and to develop the thermodynamically consistent driving forces for both slip and twinning. Dislocation based crystal plasticity with an emphasis on the interaction of all types of dislocation density in all variants is proposed, which can also be directly used for multiphase crystal materials. For twinning, the evaluation of twin concentrations governed by a resolved shear stress is utilized, and a methodology for dislocation density evolution during twinning is proposed, in which dislocation parameters in the newly formed variants at a short time period are the same as preexisting variants.

The constitutive equations for elasticity, slip and twinning are implemented into a user material subroutine (VUMAT) in the FEM code ABAQUS. The SHPB impact loading along the [0001] and $\left[10\bar{1}1\right]$ directions of single crystal titanium is simulated and compared directly with experiment. The evolutions of dislocation density, stress-strain field, and the volume fractions

for all variants in the sample during the entire loading process are obtained and discussed in detail. Results obtained from the FEM simulations show that due to the existence of six symmetry primary twin variants with respect to the loading direction and fifteen different slip systems in each variant, the fields of stress and dislocation density are very homogenous for the [0001] specimen. Plastic deformation due to slip is suggested to be the predominant deformation in the sample under SHPB, and the deformation due to slip is much larger in magnitude than the deformation due to twinning for both [0001] and $\left[10\bar{1}1\right]$ specimens. It is two orders of magnitude greater than the magnitude of elastic deformation. For the [0001] specimen, the results show that the density of pileup dislocations between prismatic and pyramidal systems in the twins can have very different trends, because the resistance stress for the escape of pileup dislocations is much larger in the pyramidal slip systems. The simulation results are compared with experimental data and very good correspondences between experiment and simulation are obtained. Multiple experimental phenomena are explained and interpreted for both [0001] and $\left[10\bar{1}1\right]$ specimens, which include the pole figures, the stress-strain curves, and volume fraction of variants, etc.

The system of constitutive equations in this paper advances the theory of coupled elasticity, plastic slip and plastic twinning under dynamic loading conditions. The simulation results provide important insight into the mechanical response of high-purity, single crystal titanium under high rate dynamical loading, where most of in-situ experimental information during rapid loading events is not currently available. This advanced model allows us to explain and interpret experimental phenomena.

Acknowledgements

The authors gratefully acknowledge support for this work from Los Alamos National Laboratory Campaign 2 Dynamic Materials program, Advanced Simulation and Computing program, and LDRD project 20150431ER. Fruitful discussions and numerical assistance from Dr. H. Mourad, and Dr. J. Mayeur is also gratefully acknowledged.

References

Abdolvand, H., Daymond, M.R., 2013. Multi-scale modeling and experimental study of twin inception and propagation in hexagonal close-packed materials using a crystal plasticity finite element approach part I: average behavior. J. Mech. Phys. Solids 61, 783-802.

Abdolvand, H., Daymond, M.R., Mareau, C., 2011. Incorporation of twinning into a crystal plasticity finite element model: Evolution of lattice strains and texture in Zircaloy-2. Int. J. Plast. 27, 1721-1738.

Abdolvand, H., Majkut, M., Oddershede, J., Schmidt, S., Lienert, U., Diak, B.J., Withers, P.J., Daymond, M.R., 2015a. On the deformation twinning of Mg AZ31B: a three-dimensional synchrotron X-ray diffraction experiment and crystal plasticity finite element model. Int. J. Plast. 70, 77-97.

Abdolvand, H., Majkut, M., Oddershede, J., Wright, J., Daymond, M.R., 2015b. Study of 3-D stress development in parent and twin pairs in of a hexagonalclosed pack polycrystal: part II --crystal plasticity finite element modeling. Acta Mater. 93, 235-245.

Abdolvand, H., Wright, J., Wilkinson, A.J., 2018. Strong grain neighbour effects in polycrystals. Nat. Commun. 9, 171.

Addessio, F.L., Luscher, D.J., Cawkwell, M.J., Ramos, K.J., 2017. A single-crystal model for the high-strain rate deformation of cyclotrimethylene trinitramine including phase transformations and plastic slip. J. Appl. Phys. 121, 185902.

Alankar, A., Eisenlohr, P., Raabe, D., 2011. A dislocation density-based crystal plasticity constitutive model for prismatic slip in alpha-titanium. Acta Mater. 59, 7003-7009.

Ardeljan, M., McCabe, R.J., Beyerlein, I.J., Knezevic, M., 2015b. Explicit incorporation of deformation twins into crystal plasticity finite element models. Comput. Methods Appl. Mech. Eng. 295, 396-413.

Arul Kumar, M., Beyerlein, I.J., Tome, C.N., 2016. Effect of local stress fields on twin characteristics in HCP metals. Acta Mater. 116, 143-154.

Asaro, R.J., Crystal plasticity. J. Appl. Mech. 50, 921-934.

Beyerlein, I.J., Tome, C.N., 2008. A dislocation-based constitutive law for pure Zr including temperature effects. Int J Plast. 24, 867-895.

Beyerlein, I.J., Capolungo, L., Marshall, P.E., McCabe, R.J., Tome, C.N., 2010. Statistical analyses of deformation twinning in magnesium. Philos. Mag . 90, 4073-4074.

Beyerlein, I.J., Tome, C.N., 2010. A probabilistic twin nucleation model for HCP polycrystalline metals. Proc. R. Soc. A 466, 2517-2544.

Beyerlein, I.J., McCabe, R.J., Tome, C.N., 2011. Stochastic processes of {1012} deformation twinning in hexagonal close-packed polycrystalline zirconium and magnesium. Int. J. Multiscale Com. 9, 459-480.

Bezruchko, G.S., Razorenov, S.V., Kanel, G.I., Fortov, V.E., 2006. Influence of temperature upon the alpha to omega transition in titanium. AIP Conf. Proc. 845, 192-195.

Bronkhorst, C. A., Kalidindi, S. R., Anand, L., 1992. Polycrystal plasticity and the evolution of crystallographic texture in fcc metals. Phil. Trans. Roy. Soc. Lond. A 341, 443-477.

Bronkhorst, C. A., Hansen, B. L., Cerreta, E. K., Bingert, J. F., 2007. Modeling the microstructural evolution of metallic polycrystal materials under localization conditions. J. Mech. Phys. Solids 55, 2351-2383.

Bronkhorst, C. A., Ross, A. R., Hansen, B. L., Cerreta, E. K., Bingert, J. F., 2010. Modeling and characterization of grain scale strain distribution in polycrystalline tantalum. Computers, Materials & Continua 17, 149-174.

Bieler, T.,Wang, L., Beaudoin, A., Kenesei, P., Lienert, U., 2014. In situ characterization of twin nucleation in pure Ti using 3D-XRD. Metall. Mater. Trans. A 45, 109-122.

Capolungo, L., Marshall, P.E., McCabe, R.J., Beyerlein, I.J., Tome, C.N., 2009. Nucleation and growth of twins in Zr: A statistical study. Acta Mater 57, 6047-6056.

Cerreta, E.K., Escobedo, J.P., Rigg, P.A., Trujillo, C.P., Brown, D.W., Sisneros, T.A., Clausen, B., Lopez, M.F., Lookman, T., Bronkhorst, C.A., Addessio, F.L., 2013. The influence of phase and substructural evolution during dynamic loading on subsequent mechanical properties of zirconium. Acta Mater. 61, 7712-7719.

Cheng, J., Ghosh, S., 2015. A crystal plasticity FE model for deformation with twin nucleation in magnesium alloys. Int. J. Plast. 67, 148-170.

Cheng, J., Ghosh, S., 2017. Crystal plasticity finite element modeling of discrete twin evolution in polycrystalline magnesium. J. Mech. Phys. Solids 99, 512-538.

Cheng, J., Shen, J., Mishra, R. K., Ghosh, S., 2018. Discrete twin evolution in Mg alloys using a novel crystal plasticity finite element model. Acta Mater. 149, 142-153.

Clayton, J.D., 2010. Nonlinear mechanics of crystals. Springer, New York.

Clouet, E., Caillard, D., Chaari, N., Onimus, F., Rodney, D., 2015. Dislocation locking versus easy glide in titanium and zirconium. Nat. Mater. 14, 931-937.

Cuitino, A., Ortiz, M. 1993. Constitutive modeling of 112 intermetallic crystals. Mat. Sci. Eng. a-Struct. 170, 111-123.

Escobedo, J.P., Cerreta, E.K., Trujillo, C.P., Martinez, D.T., Lebensohn, R.A., Webster, V.A., Gray, G.T., 2012. Influence of texture and test velocity on the dynamic, high-strain, tensile behavior of zirconium. Acta Mater. 60, 4379-4392.

Feng, B., Levitas, V.I., 2016. Effects of gasket on coupled plastic flow and strain-induced phase transformations under high pressure and large torsion in a rotational diamond anvil cell. J. Appl. Phys. 119, 015902.

Feng, B., Levitas, V.I., 2017a. Coupled Elastoplasticity and Plastic Strain-Induced Phase Transformation under High Pressure and Large Strains: Formulation and Application to BN Sample Compressed in a Diamond Anvil Cell. Int. J. Plast. 96, 156-181.

Feng, B., Levitas, V.I., 2017b. Large elastoplastic deformation of a sample under compression and torsion in a rotational diamond anvil cell under megabar pressures. Int. J. Plast. 92, 79-95.

Feng, B., Levitas, V.I., 2017c. Plastic flows and strain-induced alpha to omega phase transformation in zirconium during compression in a diamond anvil cell: Finite element simulations. Mat. Sci. Eng. a-Struct. 680, 130-140.

Feng, B., Levitas, V.I., Hemley, R.J., 2016. Large elastoplasticity under static megabar pressures: Formulation and application to compression of samples in diamond anvil cells. Int. J. Plast. 84, 33-57.

Fisher, E.S., Renken, C.J., 1964. Single-Crystal Elastic Moduli and HCP to BCC Transformation in Ti, Zr, and Hf. Phys. Rev. a-Gen. Phys. 135, A482-A494.

Frew, D.J., Forrestal, M.J., Chen, W., 2005. Pulse shaping techniques for testing elastic-plastic materials with a split Hopkinson pressure bar. Exp. Mech. 45, 186-195.

Gama, B., Lopatnikov, S., Gillespie, J., 2004. Hopkinson bar experimental technique: A critical review. Appl. Mech. Rev. 57, 223-250.

Ghosh, S., Cheng, J., 2018. Adaptive multi-time-domain subcycling for crystal plasticity FE modeling of discrete twin evolution. Comput. Mech. 61, 33-54.

Gong, J.C., Britton, T.B., Cuddihy, M.A., Dunne, F.P.E., Wilkinson, A.J., 2015. < a > Prismatic, < a > basal, and < c + a > slip strengths of commercially pure Zr by micro-cantilever tests. Acta Mater. 96, 249-257.

Gray III, G.T., 2000. Classic Split-Hopkinson Pressure Bar Testing. ASM Handb. 462-476.

Hama, T., Kobuki, A., Takuda, H., 2017. Crystal-plasticity finite-element analysis of anisotropic deformation behavior in a commercially pure titanium Grade 1 sheet. Int. J. Plast. 91, 77-108.

Hammerschmidt, T., Abrikosov, I.A., Alfe, D., Fries, S.G., Hoglund, L., Jacobs, M.H.G., Kossmann, J., Lu, X.G., Paul, G., 2014. Including the effects of pressure and stress in thermodynamic functions. Phys. Status Solidi B 251, 81-96.

Hansen, B. L., Bronkhorst, C. A., Ortiz, M., 2010. Dislocation subgrain structures and modeling the plastic hardening of metallic single crystals. Mod. Sim. Mat. Sci. Eng. 18, 055001.

Hansen, B. L., Carpenter, J. S., Sintay, S. D., Bronkhorst, C. A., McCabe, R. J., Mayeur, J. R., Mourad, H. M., Beyerlein, I. J., Mara, N. A., Chen, S. R., Gray, G. T., 2013. Modeling the texture evolution of Cu/Nb layered composites during rolling. Int. J. Plast. 49, 71-84.

Hansen, B.L., Beyerlein, I.J., Bronkhorst, C.A., Cerreta, E.K., Dennis-Koller, D., 2013. A dislocation-based multi-rate single crystal plasticity model. Int. J. Plast. 44, 129-146.

Irgens, F., 2008. Continuum mechanics. Springer, Berlin.

Javanbakht, M., Levitas, V.I., 2015. Interaction between phase transformations and dislocations at the nanoscale. Part 2: Phase field simulation examples. J. Mech. Phys. Solids 82, 164-185.

Jones, D.R., Morrow, B.M., Trujillo, C.P., Gray, G.T., Cerreta, E.K., 2017. The α–ω phase transition in shock-loaded titanium. J. Appl. Phys. 122, 045902.

Khan, A.S. Huang, S., 1995. Continuum theory and plasticity. John Wiley & Sons, Inc.

Kalidindi, S. R., Bronkhorst, C. A., Anand, L., 1992. Crystallographic texture evolution in bulk deformation processing of fcc metals. J. Mech. Phys. Solids 40, 537-569.

Kalidindi, S.R., 1998. Incorporation of deformation twinning in crystal plasticity models. J. Mech. Phys. Solids 46, 267-290.

Kalidindi, S.R., 2001. Modeling anisotropic strain hardening and deformation textures in low stacking fault energy fcc metals. Int. J. Plast. 17, 837-860.

Kumar, M.A., Beyerlein, I.J., Lebensohn, R.A., Tome, C.N., 2017. Role of alloying elements on twin growth and twin transmission in magnesium alloys. Mat. Sci. Eng. a-Struct. 706, 295-303.

Kumar, M.A., Kanjarla, A.K., Niezgoda, S.R., Lebensohn, R.A., Tome, C.N., 2015. Numerical study of the stress state of a deformation twin in magnesium. Acta. Mater. 84, 349-358.

Levitas, V.I., 1996. Large deformation of materials with complex rheological properties at normal and high pressure. Nova Science Publishers, New York.

Levitas, V.I., 2004. High-pressure mechanochemistry: conceptual multiscale theory and interpretation of experiments. Phys. Rev. B 70, 184118.

Levitas, V.I., Javanbakht, M., 2015. Interaction between phase transformations and dislocations at the nanoscale. Part 1. General phase field approach. J. Mech. Phys. Solids 82, 287-319.

Levitas, V.I., Warren, J.A., 2016. Phase field approach with anisotropic interface energy and interface stresses: Large strain formulation. J. Mech. Phys. Solids 91, 94-125.

Lieberman, E. J., Lebensohn, R. A., Bronkhorst, C. A., Rollett, A. D., 2016. Microstructural effects on damage evolution in shocked copper polycrystals. Acta Mater. 116, 270-280.

Luscher, D.J., Addessio, F.L., Cawkwell, M.J., Ramos, K.J., 2017. A dislocation density-based continuum model of the anisotropic shock response of single crystal α-cyclotrimethylene trinitramine. J Mech Phys Solids 98, 63-86.

Mayeur, J. R., Beyerlein, I. J., Bronkhorst, C. A., Mourad, H. M., Hansen, B. L., 2013. A crystal plasticity study of heterophase interface character of Cu/Nb bicrystals. Int. J. Plast. 48, 72-91.

Mescheryakov, Y.I., Divakov, A.K., Zhigacheva, N.I., Petrov, Y.A., 2000. Shock-induced alpha-omega phase transition and mechanisms of spallation in shock loaded titanium alloys. Aip Conf. Proc. 505, 439-442.

Morrow, B.M., McCabe, R.J., Cerreta, E.K., Tome, C.N., 2013. Variability in ebsd statistics for textured zirconium. Mater. Sci. Eng. A 574, 157-162.

Morrow, B.M., Lebensohn, R.A., Trujillo, C.P., Martinez, D.T., Addessio, F.L., Bronkhorst, C.A., Lookman, T., Cerreta, E.K., 2016. Characterization and modeling of mechanical behavior of single crystal titanium deformed by split-Hopkinson pressure bar. Int J Plast. 82, 225-240.

Morrow, B.M., Escobedo, J.P., Field, R.D., Dickerson, R.M., Dickerson, P.O., Trujillo, C.P., Cerreta, E.K., 2017a. Examination of the alpha-omega Two-Phase Shock-Induced Microstructure in Zirconium and Titanium. AIP Conf. Proc. 1793, 100033.

Morrow, B.M., Rigg, P.A., Jones, D.R., Addessio, F.L., Escobedo, J.P., Trujillo, C.P., Saavedra, R.A., Martinez, D.T., Cerreta, E.K., 2017b. Shock and Microstructural Characterization of the alpha to omega Phase Transition in Titanium Crystals. J. Dynamic Behavior Mater. 3, 526-533.

Nervo, L., King, A., Fitzner, A., Ludwig, W., Preuss, M., 2016. A study of deformation twinning in a titanium alloy by X-ray diffraction contrast tomography. Acta Mater. 105, 417-428.

Niezgoda, S.R., Beyerlein, I.J., Kanjarla, A.K., Tome, C.N., 2013. Introducing Grain Boundary Influenced Stochastic Effects into Constitutive Models. JOM-US 65, 419-430.

Niezgoda, S.R., Kanjarla, A.K., Beyerlein, I.J., Tome, C.N., 2014. Stochastic modeling of twin nucleation in polycrystals: An application in hexagonal close-packed metals. Int. J. Plast. 56, 119-138.

Rigg, P.A., Greeff, C.W., Knudson, M.D., Gray, G.T., Hixson, R.S., 2009. Influence of impurities on the alpha to omega phase transition in zirconium under dynamic loading conditions. J. Appl. Phys. 106, 123532.

Salem, A.A., Kalidindi, S.R., Doherty, R.D., 2003. Strain hardening of titanium: role of deformation twinning. Acta Mater. 51, 4225-4237.

Salem, A.A., Kalidindi, S.R., Semiatin, S.L., 2005. Strain hardening due to deformation twinning in alpha-titanium: Constitutive relations and crystal-plasticity modeling. Acta Mater. 53, 3495-3502.

Song, S.G., Gray, G.T., 1995. Microscopic and Crystallographic Aspects of Retained Omega-Phase in Shock-Loaded Zirconium and Its Formation Mechanism. Philos. Mag. A 71, 275-290.

Staroselsky, A., Anand, L., 1998. Inelastic deformation of polycrystalline face centered cubic materials by slip and twinning. J. Mech. Phys. Solids 46, 671-696.

Trinkle, D. R., Hennig, R. G., Srinivasan, S. G., Hatch, D. M., Jones, M. D., Stokes, H. T., Albers, R. C., Wilkins, J. W., 2003. A new mechanism for the alpha to omega martensitic transformation in pure titanium. Phys. Rev. Lett. 91, 025701.

Tome, C.N., Maudlin, P.J., Lebensohn, R.A., Kaschner, G.C., 2001. Mechanical response of zirconium—I. Derivation of a polycrystal constitutive law and finite element analysis. Acta Mater. 49, 3085-3096.

Sun, C.Y., Guo, N., Fu, M.W., Wang, S.W., 2016. Modeling of slip, twinning and transformation induced plastic deformation for TWIP steel based on crystal plasticity. Int. J Plast. 76, 186-212.

Sun, C.Y., Wang, B., Politis, D.J., Wang, L.L., Cai, Y., Guo, X.R., Guo, N., 2017. Prediction of earing in TWIP steel sheets based on coupled twinning crystal plasticity model. Int. J. Adv. Manuf. Tech. 89, 3037-3047.

Vohra, Y.K., 1978. Kinetics of Phase-Transformation in Ti, Zr and Hf under Static and Dynamic Pressures. J. Nucl. Mater. 75, 288-293.

Wang, H., Wu, P.D., Wang, J., Tome, C.N., 2013. A crystal plasticity model for hexagonal close packed (HCP) crystals including twinning and de-twinning mechanisms. Int. J. Plast. 49, 36-52.

Wang, K., 1996. The use of titanium for medical applications in the USA. Mat. Sci. Eng. a-Struct. 213, 134-137.

Wong, S.L., Madivala, M., Prahl, U., Roters, F., Raabe, D., 2016. A crystal plasticity model for twinning- and transformation-induced plasticity. Acta Mater. 118, 140-151.

Yoo, M.H., Agnew, S.R., Morris, J.R., Ho, K.M., 2001. Non-basal slip systems in HCP metals and alloys: source mechanisms. Mat. Sci. Eng. a-Struct. 319, 87-92.

Yoo, M.H., 1981. Slip, twinning, and fracture in hexagonal close-packed metals. Metall. Trans. A. 12, 409-418.

Yu, Q., Shan, Z.W., Li, J., Huang, X.X., Xiao, L., Sun, J., Ma, E., 2010. Strong crystal size effect on deformation twinning. Nature 463, 335-338.

Zecevic, M., Knezevic, M., Beyerlein, I. J., Tomé, C. N., 2015. An elasto-plastic self-consistent model with hardening based on dislocation density, twinning and de-twinning: Application to strain path changes in HCP metals. Mat. Sci. Engr. A 638, 262-274.

Zeng, Z.P., Zhang, Y.S., Jonsson, S., 2009. Deformation behaviour of commercially pure titanium during simple hot compression. Mater. Design 30, 3105-3111.

Zhang, J., Ramesh, K.T., Joshi, S.P., 2014. Stochastic size-dependent slip-twinning competition in hexagonal close packed single crystals. Model. Simul. Mater. Sc. 22, 075003.

Zong, H.X., Lookman, T., Ding, X. D., Luo, S.N., Sun, J., 2014. Anisotropic shock response of titanium: Reorientation and transformation mechanisms. Acta Mater. 65, 10-18.